Pore network modeling of reactive permeability

by

Jeffrey Hearn Steinwinder

A thesis submitted to the Graduate Faculty of
Auburn University
in partial fulfillment of the
requirements for the Degree of
Master of Science

Auburn, Alabama
May 4, 2019

Keywords: precipitation, dissolution, porosity, permeability, modeling

Approved by

Lauren E. Beckingham, Chair, Assistant Professor of Civil Engineering
Mark Barnett, Professor of Civil Engineering
Jose Vasconcelos, Associate Professor of Civil Engineering

Abstract

Geochemical reactions, such as those that occur during storage of carbon dioxide in saline aquifers as part of carbon capture and storage (CCS) mitigation techniques or long-term subsurface mineral weathering, can significantly alter the properties of porous media. Specifically, the mineral dissolution and precipitation reactions that occur may considerably change the porosity and permeability of porous media. In general, porosity increases with dissolution and decreases with precipitation. However, permeability evolution is controlled by the spatial locations of reactions in discrete pores and pore-throats and in the greater pore-network and is less understood. Additionally, reaction fronts may form as reactive fluids moves through porous media, resulting in geochemical reactions that homogenously or heterogeneously propagate through the network. Geochemical reactions have been observed to occur both uniformly and non-uniformly, driven by parameters such as mineral distribution, grain size, and flow rate. Pore network modeling can be employed to simulate the impact of pore scale alterations on permeability, requiring only pore and pore-throat size distributions and pore connectivity. Here, the impact of variations in pore and pore-throat size distributions on reactive permeability for uniform and non-uniform spatial distributions of reactions as well as the impact of reaction front gradients is evaluated. A series of pore network models are created and populated with pore and pore-throat size distributions of varying types (right-skewed, left-skewed, normal, uniform) to represent differences in network topology and characterization methods. The impacts of these distributions on reactive permeability are then simulated for uniform and non-uniform reaction conditions by increasing or decreasing pore and pore-throat sizes in a prescribed manner to reflect dissolution and precipitation,

respectively. Overall, simulations reveal that porosity-permeability evolution varies with reaction scenario and is qualitatively consistent for the different pore and pore-throat size distributions. These simulations, however, assume reactions occur to equal extents throughout the pore network. In reality, reactions may propagate with fluid flow and simulation results for propagated dissolution and precipitation reactions are constructed and compared to simulations where the entire pore network was impacted. Simulation results for all scenarios are compared with common macroscopic porosity-permeability relationships. In some cases, these relationships work well but they are unable to reflect porosity-permeability evolution when reactions initiative in small or large pores and pore-throats. In this work, a new modified version of the Verma-Pruess relationship is created that is able to successfully reflect the porosity-permeability evolution for size dependent reactions.

Acknowledgments

This work is supported by Auburn University in part through the Presidential Awards for Interdisciplinary Research (PAIR) program. The author would like to thank his advisor, Dr. Lauren Beckingham, for all of her patience and guidance during the past two years. She has truly been a great mentor while always being fair and honest in all discussions. As well as the advisory committee, the author thanks Dr. Mark Barnett and Dr. Jose Vasconcelos for their thoughtful feedback and assistance in completion of this task. The author also thanks his research team members, Fanqi, Chidera and Ishan, for long drawn-out research discussions and expanding his knowledge of other cultures through food and music. The author also thanks his fiancé, Mattie, and family for their love and support over the past two years, they have truly made a difference.

Table of Contents

List of Tables

List of Figures

List of Abbreviations

CCS	Carbon Capture and Storage
CCUS	Carbon Capture, Utilization and Storage
Da	Damköhler number
GHG	Greenhouse Gas
IR	Infrared Radiation
Pe	Péclet number
PNM	Pore Network Model
REV	Representative Elementary Volume

Chapter 1

Introduction

1.1 Background

Atmospheric carbon-dioxide (CO_2) has increased more than 40% since the industrial revolution (NAS, 2014) and continues to rise (Keeling, 1976). The rising concentration of atmospheric CO_2 has prompted public concerns due to increased climate variability and intensity. In particular, near-surface ambient temperatures have increased by 1.4°F since the early twentieth-century, attributed mainly to anthropogenic burning of fossil fuels (e.g. IPCC, 2007; NAS, 2014) as well as land use change such as deforestation (e.g. IPCC, 2000). The Intergovernmental Panel on Climate Change (IPCC) stated in its fourth assessment report that greenhouse gas (GHG) emissions have grown ”70% between 1970 and 2004”, where most of the observed global temperature increase since the mid-1900s is very likely due to an increase of anthropogenic GHG concentrations (IPCC, 2007). Examples include coal-fired power plants for utility-scale power production and preparation of natural-gas (IPCC, 2005). When combusted, fossil fuels produce GHGs including methane (CH_4), water vapor (H_2O), nitrous oxide (N_2O) and ozone (O_3); however, the primary driver in global temperature change is CO_2 due to abundance and warming potential (cite). Increased atmospheric CO_2 traps outgoing infrared radiation (IR) from Earth’s surface driving a shift in energy balance (e.g. radiative forcing) and subsequent increase in near surface global temperatures (Archer et al., 2009; Hansen et al., 2005).

1.2 Carbon Capture, Utilization and Storage (CCUS)

Efforts to combat the rise in atmospheric CO_2 coupled with global temperatures include a myriad of mitigation and emissions reduction techniques, referred to as carbon capture, utilization and storage (CCUS). CCUS provides a technically feasible and interdisciplinary approach to initial CO_2 capture from large point-sources (e.g. industry or power-production facilities), transport to a storage site, and long-term storage in deep geologic formations, oceans, or use in industrial processes (Figueroa et al., 2007; IPCC, 2005). These mitigation techniques could decrease net CO_2 emissions from sources such as power generation and cement production, the two largest CO_2 emitters, where observed annual emissions are 10,539 $MtCO_2$ and 932 $MtCO_2$, respectively (IPCC, 2005). Initial capture of CO_2 from industrial or power-production applications is typically carried out by scrubbing-unit operations (Audus et al., 1996; Siddique, 1990) or by more novel removal approaches such as pressure swing adsorption for natural gas (Tao et al., 2019). Then, CO_2 is transported as a compressed gas with a volume decreased by approximately 98% as compared to that of gaseous CO_2 at standard conditions (IPCC, 2005). CO_2 is then injected into a deep geologic formation for long-term storage. To be selected for long-term storage of CO_2, reservoirs must meet specific criteria to ensure efficient injection and safe storage. Suitable reservoirs must have a large capacity and enable high injectivity to ensure reservoirs can receive the desired CO_2 volume at the specified injection rate from CCS facilities. Formations also require proper confinement to ensure injected CO_2 can be stored without leakage to nearby groundwater zones or to the surface (Bachu, 2008). Desired aquifer depths are those where CO_2 will exist as a supercritical fluid with a higher density, and thus potential storage volume. Supercritical CO_2 is immiscible in water and significantly less viscous than residual formation fluid (IPCC, 2005) driving heterogeneous plume

formation, transport and trapping. Once injected, CO_2 will mix with the residual reservoir brine fluid forming a low pH CO_2-brine solution, thus developing a reactive environment where CO_2 may be mineralized as calcium carbonate ($CaCO_3$) (e.g. Oelkers et al., 2008), and reservoir rock may be dissolved. Nonetheless, CO_2 mineralization is not the only method of safe long-term storage.

1.3 Trapping Mechanisms

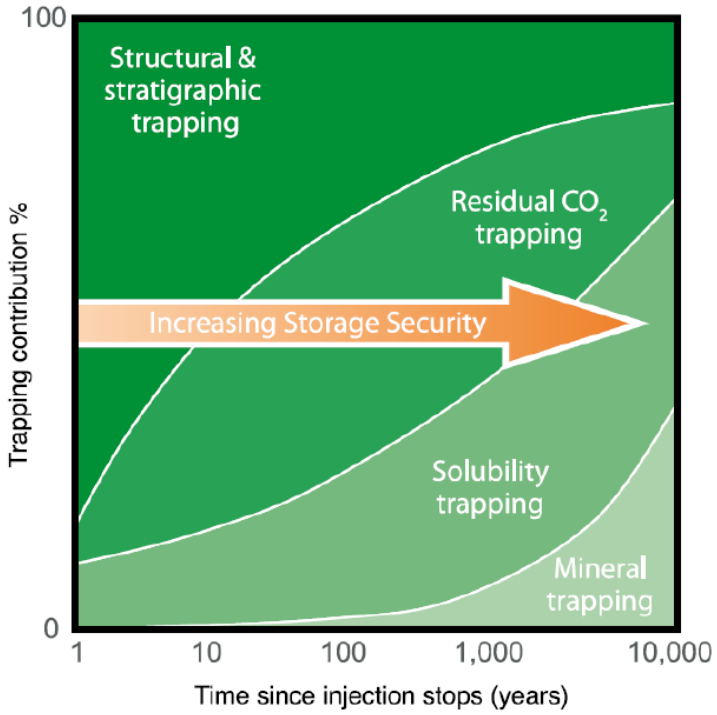

Figure 1 - Schematic from CO_2 CRC (2013) showing a series of trapping mechanisms during geologic sequestration of CO_2

As a CO_2 plume propagates from the injection well, a series of trapping mechanisms may occur at reservoir conditions, typically 10 MPa and 50°C (e.g. Menke et al., 2017), promoting the storage of injected CO_2, shown in Figure 1 (CO2CRC, 2013). Trapping mechanisms are observed to be a function of time in the reservoir, typically beginning with structural trapping, proceeding to

residual trapping and solubility trapping, where CO_2 is trapped in pore spaces due to capillary pressure and dissolved in residual brine, respectively (e.g. Bachu, 2000; Singh et al., 2019). In consideration of enhanced storage security, mineral trapping, where CO_2 precipitates as new carbonate minerals, yields the lowest risk of leakage (e.g. CO2CRC, 2013) and ensures compliance with a stated policy goal (e.g. IPCC, 2005). While mineral trapping is typically shown to occur on timescales greater than 10,000 years, these estimates are largely erroneous as they do not account for reactive surface area, pH fluctuations, and fluid composition which can result in orders of magnitude in the time estimates of mineral reactions (Xu et al., 2010). In field studies, mineralization has been shown to occur over a short distance from injection well (Tenthorey et al., 2011). Observations at CarbFix, an industrial-scale process for removing CO_2 emissions from Hellisheidi geothermal power plant in Iceland and injecting into subsurface formations, observed mineralization within 12 months of injection (Gislason et al., 2018). It should be noted, however, that the CarbFix project injected CO_2 saturated brine as opposed to gaseous CO_2 (Snaebjornsdottir et al., 2017). Mineralization of dissolved CO_2 into carbonate rock results from deviations in geochemical equilibrium that drive dissolution and precipitation reactions in individual pores and the greater pore-network. For example, the dissolution of anorthite and precipitation of calcite and kaolinite, from Oelkers et al. (2008), is shown in Equation 1.1 as

$$CaAl_2Si_2O_8 + CO_2 + 2H_2O \rightarrow CaCO_3 + Al_2Si_2O_5(OH)_4 \quad (1.1)$$

1.4 Role of pore and pore-throat size distributions in controlling permeability in heterogeneous mineral dissolution and precipitation scenarios

The fate and transport of CO_2 injected in geologic formations relies on the porous media properties, such as porosity and permeability, which can be impacted by geochemical dissolution

and precipitation reactions (e.g. Equation 1.1). During injection, these reactions can occur uniformly and nonuniformly throughout the porous media, controlled by pore and pore-throat size distributions and flow rate, for example. The pore and pore-throat distributions have been observed to cause variations in porosity and permeability in both modeling simulations (e.g. Emmanuel et al. 2010; Lamy-Chappuis et al., 2018) and laboratory experiments (e.g. Ishutov et al., 2017; Mangane et al., 2013; Menke et al., 2017; Tenthorey and Scholz, 2002), where reactions tend to be dependent on the size of individual pore and pore-throat (e.g. Figure 2) as well as the overall size distribution. The evolution of porosity and permeability are also driven by the spatial distribution of reactions in the pore network, where Beckingham (2017) observed uniformly distributed reactions to drive a change in porosity coupled with a similar change in permeability, although non-uniformly distributed reactions (e.g. reactions dependent on pore and pore-throat size) drive non-linear changes in porosity and permeability. These observed variations are extremely important for prediction of a selected reservoir's capacity and injectivity for CCUS, which may change over the course of an injection period (Bacci et al., 2011a,b; Oelkers et al., 2008; Voltolini and Ajo-Franklin, 2019). In order to study the evolution of reactive permeability in a large range of possible pore and pore-throat size distributions reflecting variations due to sample properties or analysis methods, three synthetic distribution are created. The effect of the spatial location of dissolution and precipitation reactions on porosity-permeability evolution as well as the effect of varying pore and pore-throat size distributions is then evaluated through pore network modeling simulations. Simulated permeability results are then compared to common macroscopic porosity-permeability relationships. Our research purpose here is to evaluate the evolution of porosity and permeability when sample pore and

pore-throat size distributions are varied and then to compare these results to common macroscopic relationships to determine applicability of relationships.

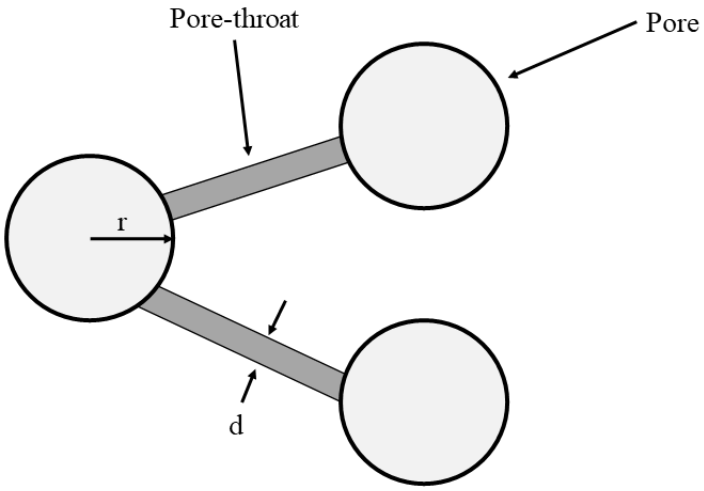

Figure 2: A schematic of pores of radius 'r' and connected by pore-throats of diameter 'd'.

1.5 Evolution of reactive permeability in geochemical reactive front propagation scenarios

Once injected, CO_2 migrates into the reservoir at high pressure and flow rates near the inlet with large net dissolution of minerals, where dissolution capacity decreases as the distance from inlet increases (e.g. Voltolini and Ajo-Franklin, 2019). Mineral trapping employs both dissolution and precipitation reactions regimes, where the former may occur near the injection well and the latter at some distance away from the well-bore. In general, porosity of a porous media controls the storage capacity and injectivity is controlled by permeability. In reactive conditions resulting from CO_2 injection, porosity and permeability may evolve where decreases and increases occur due to precipitation and dissolution, respectively (Beckingham, 2017; Crandell et al., 2012; Souliane et al., 2017). During and after injection, CO_2 migrates through the reservoir (e.g.

Hodneland et al., 2019; Jayne et al., 2019; Williams et al., 2018), creating a reactive front where conditions are favorable for mineral reactions to occur. The extent of reaction may be uniform (e.g. Voltolini and Ajo-Franklin, 2019; Menke et al., 2017) or vary by some gradient (e.g. Egermann et al., 2004; Peuble et al., 2019; Vialle et al., 2014) over a given distance. Our research purpose here is to investigate the possibility of migration simulations in a pore network model and to analyze the evolution of porosity and permeability.

Chapter 2

Role of pore and pore-throat distributions in controlling permeability in heterogeneous mineral dissolution and precipitation scenarios

J.H. Steinwinder[1], L.E. Beckingham[1*]
[1]*Auburn University, Auburn, AL 36849*
**Department of Civil Engineering, Auburn University, Auburn, AL 36849, leb@auburn.edu*

Submitted for publication in Water Resources Research.

2.1 Introduction

Mineral dissolution and precipitation reactions in porous media, such as those that occur during geologic CO_2 sequestration in saline aquifers, enhanced oil recovery, or natural weathering processes (e.g. Ketzer et al., 2009; Kump et al., 2000; Noiriel et al., 2004) may result in changes in porosity and permeability. Typically, porosity increases with dissolution and decreases with the precipitation of secondary minerals. The impact of these reactions on permeability, however, is not well understood and difficult to predict.

Large variations in the porosity and permeability of porous media subjected to reactive environments have been observed with increasing porosity coupled to increases, decreases and little change in permeability. Carbonate dissolution experiments in Khather et al. (2017), for example, resulted in increases of porosity and permeability in a low permeability sample and decreases in porosity and permeability in a similar vuggy sample as a result of physical compaction. In Rötting et al. (2015), a calcite dominate limestone sample reacted with dilute hydrochloric acid increased porosity by 2.6-5.8% with little change in permeability. Core flooding

experiments in the context of geologic CO_2 sequestration in Al-Yaseri et al. (2017) resulted in minimal change in permeability for high clay content sandstones (Bandera Grey) and increases in permeability for low clay content sandstones (Berea) with minimal change in porosity for both samples. Large changes in permeability have also been observed with little change in porosity (Noiriel, 2004; Al-Khulaifi et al., 2018). A dolomite core-flood experiment with $scCO_2$ saturated brine at reservoir conditions in Al-Khulaifi et al. (2018) resulted in an increase in porosity of 0.25% and a several orders-of-magnitude increase in permeability at low-flow conditions (0.5 ml/min). Precipitation of kaolinite in highly localized main flow paths following dissolution of sandstone samples in acid percolation experiments in Luquot et al. (2012) resulted in a one order-of-magnitude decrease in permeability with a small increase in porosity.

Permeability evolution is controlled by the location of geochemical reactions in individual pores and the larger pore network. Previously, geochemical reactions have been observed to occur uniformly and non-uniformly, influenced by the physical and chemical characteristics of porous media including pore size, grain size, and mineral distribution. Non-uniform reactions have been observed to occur randomly distributed, along preferential flow channels, and preferentially in small or large pore and pore-throats. The distribution of reactive minerals controlled the crystallization location and growth rates in experiments in Noiriel et al. (2016) where reactive minerals may be randomly distributed (e.g. Beckingham et al. 2013). Channelized reactions have been observed in several previous experiments, occurring along preferential flow channels and often resulting in worm hole formation (e.g. Deng et al., 2015; Luquot et al., 2012; Menke et al., 2016). In regards to pore and pore-throat sizes, it has been suggested that reactions may preferentially occur or be inhibited in both small or large pores and pore-throats. Mineral precipitation has been experimentally observed to be favored in narrow pore-throats (Tenthorey

and Scholz 2002) while numerical simulations have suggested interfacial energy effects in small pore volumes may inhibit reactions in small pores (e.g. <10 microns) (Emmanuel et al. 2010). Other experiments have observed mineral reactions to be independent of sample characteristics and observed reactions occurring uniformly on all grain surfaces, as with sodalite/cancrinite precipitates on Hanford grain surfaces in Crandell et al. (2012). Pore network modeling simulations in Beckingham (2017) considered the impact of the spatial distribution of mineral reactions on porosity and permeability and found large variations in the evolution of permeability depending on reaction locations.

The extent of geochemical reaction also influences porosity and permeability evolution and has shown an observed dependence on flow rates. Replicate dolomite dissolution experiments carried out with varied flow-rates resulted in an increase in permeability at flow rates of 0.1 ml/min and decrease at flow rates of 0.01 ml/min due to the respective decrease in relative reaction kinetics (Luhmann et al., 2014). The coupling between flow rates and reactivity is often described using the Peclet (Pe) and Damkohler (Da) numbers that quantify the ratio of advection and diffusion, and reaction and diffusion, respectively. High Da scenarios (e.g. high reaction rates relative to fluid transport rates) are linked to non-uniform alterations to the pore matrix, including channeling and worm-holing (Noiriel, 2015, Qi et al., 2018). For slow reaction kinetics compared to fluid transport (low Da values), dissolution is observed to occur uniformly (Golfier et al., 2002; Tartakovsky et al., 2007). This is supported by simulations in Soulaine et al. (2017) where Da values less than 1 are classified as a uniform dissolution regime and mineral dissolution reactions occur homogenously.

In general, porosity is dominated by pore bodies while permeability is controlled by pore-throats such that changes in pores largely impact porosity and changes in pore-throats impact

permeability (e.g. Crandell et al., 2012; Luhmann et al., 2017). A reduction in the size and number of flow conducting pore-throats due to uniform mineral precipitation in Crandell et al. (2012), for example, resulted in a decrease in network permeability. The heterogeneity of pore and pore-throat size distributions may also impact porosity and permeability evolution (Smith et al. 2013, Hao et al. 2013, Bashtani et al. 2018). Reactive flow-through experiments in Smith et al. (2013) resulted in pore distributions becoming increasingly heterogeneous and larger variations in mass transfer rates, resulting in the formation of unstable reactive fronts and an increase of permeability of several orders-of-magnitude. Numerical simulations in Hao et al. (2013) suggest that pore space heterogeneity influences permeability variability, where dissolution fronts become less uniform and favor development of wormholes as heterogeneity increases. Additional complexities, such as surface roughness, confining stress, salinity, and acidity have also been shown to impact permeability evolution (Ishibashi et al., 2013, Al-Yaseri et al. 2017).

Pore-scale modeling has developed as an effective way to analyze flow properties in porous media including permeability. Two primary pore-scale simulation methods are typically used: pore-network modeling and lattice Boltzman simulations (Lichtner and Kang, 2007). Pore network modeling, originally developed by Fatt (1956), has emerged as a valuable tool to simulate up-scaled mineral reaction rates (e.g. Li et al. 2006, Varloteaux et al. 2013) and porosity-permeability evolution in heterogeneous porous media (e.g. Bashtani et al., 2018; Beckingham 2017; Nogues et al., 2013). In these models, multi-directional pore networks are discretized on a regular or irregular cubic lattice of nodes (pores) and connections (pore-throats). Laminar flow of an incompressible fluid, driven by an applied macroscopic pressure gradient across the system, is then simulated (e.g. Algive et al., 2012; Beckingham et al. 2013; Beckingham 2017; Kim et al., 2011; Li et al. 2006; Raoof and Hassanizadeh, 2009; Varloteaux et al., 2013; Xiong et al., 2016).

Compared to other pore-scale simulation methods (e.g. lattice Boltzman, smooth particle hydrodynamics), pore network models are computationally efficient, producing a simplified porous structure for analysis (Lindquist et al. 2000; Varloteaux et al., 2013). In addition, pore-network models have the advantage of not depending on constitutive relationships to determine structural evolutions, a major limitation of continuum scale reactive transport models. These relationships are commonly empirical in nature and developed using bulk averaging approaches and are limited in applicability (e.g. Beckingham 2017). Pore-to-core scale reactive transport and resulting changes in individual pores, pore-throats and the greater pore network are easily simulated in pore network models, requiring only pore and pore-throat size distributions and pore connectivity to develop the model.

Pore and pore-throat size distributions can be obtained through a variety of methods including laboratory and 2D and 3D imaging methods (e.g. Beckingham et al. 2013; Niu and Zhang et al., 2017; Xiong et al., 2016; Xiao et al., 2017; Zhang et al., 2017). Common laboratory methods include Mercury Injection Capillary Pressure (MICP) and low-field Nuclear Magnetic Resonance (NMR). These techniques, however, have shown to be inconsistent, resulting in discrepancies in measured pore network properties. Zhang et al. (2017) compared NMR and MICP measurements for shale samples and found MICP resulted in higher porosities than NMR and imaging methods (7.94% versus 4.89%). This discrepancy may have resulted from a large volume of artificial pores due to structural modifications (e.g. deformation of the initial sample pore structure) during the intrusion test (Zhang et al. 2017). It should also be noted that MICP measurements reflect pore-throat sizes, versus pore bodies, and are unable to account for isolated pores (Lai et al., 2017).

Image analysis methods typically include 2D Scanning Election Microtomography (SEM) and 3D X-ray computed tomography (X-ray CT) images where the pore network is characterized

using statistical, grain-based, or direct mapping methods (Anovitz and Cole, 2015; Xiong et al., 2016). Pores are identified in 2D SEM or 3D X-ray CT images by first segmenting images into pore and grain pixels based on pixel intensities or voxel attenuation values (e.g. Peters 2009). Segmented images are then processed using a variety of techniques to classify pore and pore-throat sizes. Methods for obtaining pore and pore-throat size distributions from 2D images include image erosion-dilation (e.g. Crandell et al., 2012) and multiple point statistics (e.g. Okabe and Blunt, 2004). 2D image analysis techniques require a bias correction, based on stereology theory (e.g. Wiebel, 1979), and supplemental 3D image information to determine pore connectivity (e.g Crandell et al., 2012). Pore and pore-throat size distributions are typically extracted from 3D images using the medial axis or maximum ball techniques (Lindquist et al. 1996, Yi et al. 2017) and more accurately reflect 3D object characteristics (e.g. connectivity). Errors in pore and pore-throat size distributions determined from images may result from partial volume effects or limitations of image resolution (e.g. Anovitz and Cole 2015, Steefel et al. 2015, Shah et al., 2016, Beckingham et al., 2013).

While large variations in pore and pore-throat size distributions and connectivity may result from different measurement techniques, pore and pore-throat size distributions for sandstones are typically statistically right-skewed. In these distributions, the average pore and pore-throat size is larger than the respective median values, indicative of a higher frequency of small pores and pore-throats (Beckingham et al., 2013; Bloomfield et al., 2001; Doyen, 1988; Lindquist et al., 2000; Øren and Bakke, 2003; Saadi et al., 2017). Image resolution limitations, however, may underestimate small pores and pore-throats. Pore and pore-throat size distributions also depend on the sample characteristics where different sample types may have different pore and pore-throat size distributions. Pore size distributions for sand packed columns in Cil et al. (2017), for example,

are normally distributed. While it is generally understood that pore and pore-throat size distributions influence macroscopic flow properties (e.g. Ehrlich et al. 1984), the influence of variations in these distributions on reactive porosity and permeability evolution is unknown.

In this study, the impact of pore and pore-throat size distributions on reactive permeability evolution is investigated using pore network model simulations. Three synthetic pore and pore-throat size distributions are created and used to populate pore network models. Pore network models are then subjected to uniform and non-uniform mineral reactions and changes in porosity and permeability are simulated. Simulated results are compared to similar simulations carried out for a sandstone sample in Beckingham (2017) and common macroscopic porosity-permeability relationships.

2.2 Materials and Methods

2.2.1 Pore and pore-throat size distributions

2.2.1.1 Alberta basin sandstone

Pore and pore-throat size distributions and reactive pore network modeling simulations for a Viking sandstone sample from the Alberta basin are considered here for comparison purposes. This sample has been the focus of several previous investigations where the sample composition was considered in Peters (2009), pore and pore-throat-size distributions determined in Kim et al. (2011) and Beckingham et al. (2013), and reactive pore network modeling simulations carried out in Beckingham (2017). This sample, termed "3w4", has a porosity of 14-18% as determined from SEM and X-ray CT and imaging analyses in Peters (2009) and Kim et al. (2011). The permeability, measured by probe permeameter in Beckingham et al. (2013), ranges from 2.4×10^{-13} to 4.5×10^{-13} m^2. This sandstone, is predominantly quartz (73 +/- 3%) with 21 +/- 2% Mg chlorite, kaolinite, montmorillonite and albite and 5 +/- 1% accessory minerals (dolomite, illite, K-spar, anorthite,

calcite, apatite, biotite, Fe chlorite, siderite, Ti and Fe oxides, and pyrite), as determined using SEM imaging in Peters (2009).

Pore and pore-throat size distributions of sample 3w4 were determined using 2D SEM backscattered electron (BSE) and 3D X-ray CT imaging in Beckingham et al. (2013) and Kim et al. (2011), respectively. Distributions were determined from 2D images using an image erosion-dilation analysis in Beckingham et al. (2013) and from 3D images using 3DMA-Rock in Kim et al. (2011). In this study, the 3D dataset will be used. The pore and pore-throat size distributions, shown in Figure 1A, are right-skewed and contain a large frequency of small pores and pore-throats, agreeing with other previous sandstone sample observations (Bloomfield et al., 2001; Doyen, 1988; Lindquist et al., 2000; Øren and Bakke, 2003; Saadi et al., 2017). The mean pore and pore-throat sizes are 28.02 μm and 15.92 μm, respectively, with standard deviations of 14.23 μm and 12.62 μm, respectively. The maximum pore and pore-throat sizes are 235.83 μm and 137.31 μm, respectively, while the respective minimum values are 4.94 μm and 2.25 μm.

2.2.1.2 Synthetic distributions

Pore and pore-throat size distributions are influenced by the measurement method where variations in distributions result from different measurement approaches (e.g. laboratory MICP versus imaging analysis) (Anovitz and Cole, 2015; Noiriel, 2015; Xiong et al., 2016; Zhang et al., 2017). To capture this variation, additional synthetic pore and pore-throat size distributions are created here to capture the largest possible variations in size distributions. This includes left-skewed, uniform, and normal pore and pore-throat size distributions. Distribution parameters (e.g. maximum and minimum pore and pore-throat size) are set such that the pore network model

simulated initial porosity and permeability (Section 2.2) matches that of sandstone 3w4. Minimum and maximum pore and pore-throat sizes are set to match those of 3w4 when possible.

Left-skewed distributions were created by mirroring the 3w4 pore and pore-throat size distributions, resulting in distributions with a higher frequency of large pores and pore-throats and lower frequency of small pores and pore-throats. Left-skewed distributions represent samples with predominately large pores and pore-throats, where the means of the pore and pore-throat size distributions are less than their respective median and mode values. The minimum pore and pore-throat sizes are set to match those of sandstone 3w4 and the maximum pore and pore-throat sizes are set to 50 µm to match the simulated initial porosity and permeability (Section 2.2) of 3w4.

Uniform pore and pore-throat size distributions correspond to an equal frequency of all pore and pore-throats sizes and were established here by defining a constant probability density function as given by,

$$P(x) = \begin{cases} 0 & for\ x < a \\ \frac{1}{b-a}\,\eta & for\ a \le x \le b \\ 0 & for\ x > b \end{cases} \tag{2.1}$$

where a is the minimum pore or pore-throat radii, b is the maximum pore or pore-throat radii, and η is a constant to increase the magnitude of frequency. The minimum pore and pore-throat sizes match those of sample 3w4, where the maximum values were set at 50 µm to match simulated initial porosity and permeability of the 3w4 sample.

The normal pore and pore-throat size distributions were created using the mean for the 3w4 pore and pore-throat size distributions and the Microsoft EXCEL normal distribution function multiplied by a constant to increase frequency magnitude. The minimum and maximum pore and pore-throat sizes were set to match those of sandstone 3w4.

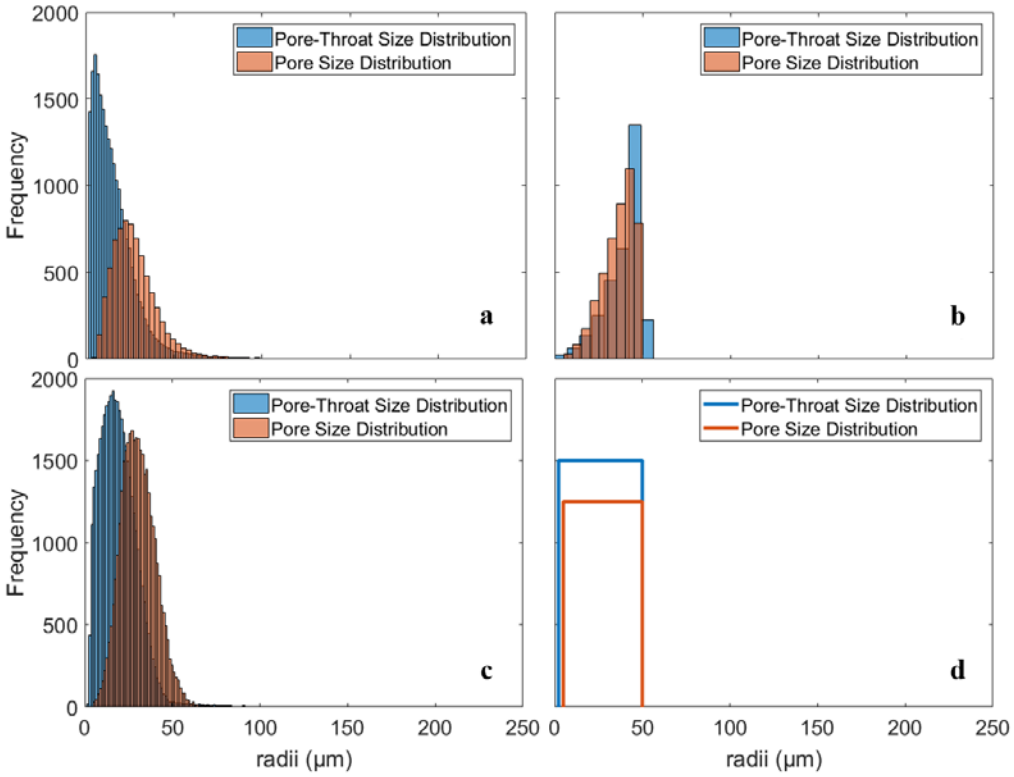

Figure 3. Pore and pore-throat size distributions to be used in pore network modeling simulations including (a) right-skewed distributions for sample, modified from Beckingham et al. (2013); (b) synthetic left-skewed distributions; (c) synthetic normal distributions; and (d) synthetic uniform distributions.

2.2.2 Pore Network Modeling

Pore network modeling was used to simulate permeability following the work of Beckingham (2017) where simulations build on the pore network model developed in Li et al.

(2007) and Beckingham et al. (2013). Here, a 10 x 10 x 10 grid containing a total of 1000 nodes, or pores, was defined on a regular, cubic lattice, corresponding to physical size of approximately a 2 mm cube. The use of regular cubic lattices was validated in Arns et al. (2004). Pores were represented as idealized smooth spheres and pore-throats as smooth cylinders where pore and pore-throat radii were randomly sampled from pore and pore-throat size distributions. Nodes were connected by pore-throats where a maximum of 26 connections was allowed for each pore, after the model proposed by Raoof and Hassanizadah (2009) and shown in Figure 4. Pore coordination depends on pore size where a minimum of 2 connections and a maximum of 26 were allowed and the coordination number-pore size relationship for sample 3w4 determined in Kim et al (2011) was used for all simulations. Flow was simulated by applying a pressure differential across the entire network and permeability, *K*, inferred from Darcy's law as given by,

$$K = \frac{Q_T v L}{\Delta P \Lambda} \tag{2.2}$$

where Q_T is the total flow rate through the system, L is the network length, and Λ is the cross-sectional area of the network, v is the dynamic fluidviscosity, and ΔP is the pressure differential between the inlet and outlet (Li et al., 2007). The total flow through the network was determined by summing the flow from pore-throats at the outlet where the flow between two connected pores was given by,

$$Q_{ij} = C_{ij}(P_i - P_j) \tag{2.3}$$

where P_i and P_j is the pressure in pores i and j, respectively, and C_{ij}, is the conductance of the pore-throat connecting pore i to pore j (Li et al. 2006). The conductance was given by Hagen-Pouseuille's law for incompressible fluid flow

$$C_{ij} = \frac{\pi d_{ij}^4}{128 v l} \tag{2.4}$$

where v is dynamic viscosity, l is the pore-throat length and d_{ij} is the pore-throat diameter after Li et al. (2007). This pore network model was used to simulate permeability for the 3w4 sandstone sample in Beckingham et al. (2013) where the simulated permeability was validated, and agreed, with experimentally measured values. This model was also used to simulate reactive changes in permeability for sandstone 3w4 in Beckingham (2017) where similar simulations were carried out in this work using the synthetic pore and pore-throat size distributions to construct the pore network model and compared to results from sample 3w4.

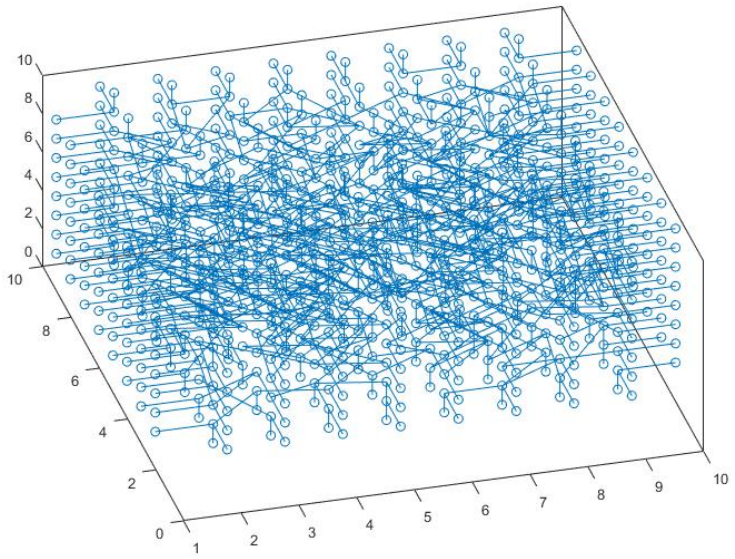

Figure 4: Representation of pore network model where pores (circles) are connected by pore-throats (lines) with a maximum connection of 26 per pore.

2.2.3 Mineral Dissolution and Precipitation Reaction Scenarios

Uniform and non-uniform spatial distributions of mineral dissolution and precipitation reactions were considered here. For each reactive simulation (e.g. sub-scenario), the radii of impacted pores and pore-throats sizes in the pore network model were increased or decreased to

reflect mineral dissolution or precipitation, respectively. 1000 simulations were carried out for each sub-scenario with varying reaction extents. The uniform and non-uniform reaction conditions considered here are the same as those carried out for reactive pore network modeling simulations for sample 3w4 in Beckingham (2017).

2.2.3.1 Uniform Reactions

Uniform mineral dissolution and precipitation reactions have been observed in previous experimental studies (e.g. Crandell et al., 2012; Smith et al., 2013; Menke et al., 2016) and numerical simulations (e.g. Beckingham 2017; Varloteaux et al., 2013), and are expected to occur in samples with homogeneous pore distributions (Hao et al., 2013; Smith et al., 2013) and under diffusion dominated (high Pe) regimes (e.g. Al-Khulaifi et al., 2018; Hoefner & Fogler, 1988; Nogues et al., 2013). Here, uniform dissolution and precipitation was simulated by assuming all pores and pore-throats were impacted by reactions. Two uniform reaction conditions were simulated where the first considered reactions that resulted in alterations of a uniform thickness and the second considered reactions that occurred to an extent related to individual pore and pore-throat sizes. Dissolution and precipitation reactions were simulated by increasing or decreasing pore and pore-throats, respectively, by a set amount (e.g. a 1 μm, 5μm or 10 μm) or a set extent relative to their unaltered size (e.g. 10%, 20% or 30% of pore or pore-throat unaltered size), as in Beckingham (2017). Reaction thicknesses ranging 1-10 μm and extents from 10-30% were simulated.

2.2.3.2 Non-Uniform Reactions

Non-uniform spatial distributions of mineral dissolution and precipitation, including random, channelized and size-dependent reactions, have been observed in previous investigations and are considered here. Nagy & Lasaga (1993) and Noriel et al. (2016), for example, observed precipitation on like mineral surfaces, which will result in a random distribution of reactions given that reactive minerals are randomly distributed throughout the pore-matrix (e.g. Beckingham et al. 2017). This scenario was simulated by increasing or decreasing randomly sampled pores and pore-throats by 20% of their original size where the fraction of reacted pores and pore-throats was varied from 10 to 40% of all pores and pore-throats.

Channelized, or "wormhole" reaction scenarios have been observed to develop in highly reactive, low diffusion, high advection conditions (high Da, low Pe) and in heterogeneous porous media (e.g. Noiriel, 2015; Smith et al. 2013). This reaction scheme was simulated by considered reactions in pores and pore-throats within a 3 x 3 x 10 system of pores aligned with the flow direction. Varying extents of dissolution and precipitation, from 10% to 50% of original pore and pore-throat sizes, were simulated.

Size-dependent reactions have been observed in numerical simulations where precipitation was inhibited in small pores due to interfacial energy effects in Emmanuel et al., (2010) and dissolution preferentially occurred in large pores under diffusion limited conditions in Varloteaux et al. (2013), for example. Experimentally, Wang et al. (2010) observed that halite precipitation only occurred in brine occupied pores where later analysis of this experimental study revealed brine primarily occupied small pores (Liu et al., 2013). Here, size-dependent reaction scenarios considering dissolution and precipitation reactions initiating in small or large pores were simulated. This was achieved by increasing or decreasing pore and pore-throat radii less-than or greater-than a reference size to reflect mineral dissolution or precipitation, respectively. A reaction

extent of 20% was considered for dissolution and precipitation. For reactions initiating in small pores and pore-throats, simulations considered reactions occurring in pores and pore-throats with radii less than 30, 40, and 50 μm. For reactions initiating in large pores and pore-throats, simulations considered reactions occurring in pores and pore-throats with radii greater than 5, 10, 25, and 45 μm.

2.2.4 Macroscopic Porosity-Permeability Relationships

Pore-network model simulated porosity-permeability was compared with commonly used continuum-scale porosity-permeability relationships. Three common macroscopic porosity-permeability relationships were considered, the Kozeny-Carman, modified Fair-Hatch, and Verma-Pruess equations. The Kozeny-Carman equation is given by

$$K = \frac{\Phi^3 d^2}{36k(1-\Phi)^2} \tag{2.5}$$

where Φ is the porosity, K is the calculated permeability, d is the mean particle diameter, and $k = c\,\tau^2$ were c is the Kozeny constant and τ is tortuosity (Carman, 1937, 1939; Kozeny, 1927). The Kozeny constant was fit to match the initial porosity and permeability for each synthetic pore and pore-throat size distribution.

A modified version of the Fair-Hatch relationship, originally derived by Bear (1972), was used here as given by

$$\frac{K(\phi)}{K_o} = \left(\frac{\phi}{\phi_o}\right)^3 \left(\frac{(1-\phi_o)^{\frac{2}{3}} + E_1(\phi_f - \phi_o)^{\frac{2}{3}}}{(1-\phi)^{\frac{2}{3}} + E_1(\phi_f - \phi)^{\frac{2}{3}}}\right)^2 \tag{2.6}$$

where Φ_0 is the initial porosity, Φ_f is final porosity after dissolution of soluble grains, E_1 is a constant after Chadam et al. (1986). The initial porosity and permeability for each synthetic pore

and pore-throat size distribution was obtained by averaging pore network model simulation results for unaltered porosity and permeability scenarios. The final porosity value, Φ_f for all synthetic pore and pore-throat size distributions was set to match that of sample 3w4, 0.345, where the final porosity reflected dissolution of all non-quartz grains (Beckingham 2017). A value of 0.7 was used for constant E_1, in agreement with Beckingham (2017).

The Verma-Pruess porosity-permeability relationship, derived in Verma and Pruess (1988), is given by,

$$\frac{K(\phi)}{K_o} = \left(\frac{\phi - \phi_c}{\phi_o - \phi_c}\right)^n \tag{2.7}$$

where Φ_0 is the initial porosity, Φ_c is the critical porosity where permeability is reduced to zero, n is an empirical power law exponent (Verma and Pruess, 1988). Values of n of 1 and 2, were considered and referred to as Verma-Pruess1 and Verma-Pruess2. The critical porosity value was calculated as 30% of the initial porosity, or 0.3 Φ_0, where initial porosity and permeabilities were determined from unaltered simulations for each pore and pore-throat distribution.

These macroscopic relationships are quantitatively compared by calculating the mean absolute error ratio (MAER) for each calculated and simulated permeability value, shown below as Equation 2.8,

$$MAER = \frac{\Sigma\left|\frac{x_{calc} - x_{sim}}{x_{sim}}\right|}{n^2} \tag{2.8}$$

Where x_{calc} is the predicted permeability values calculated by common macroscopic relationships, x_{sim} is the simulated permeability value from the PNM. The sample size, denoted as n, is 1000 for each reaction sub-scenario.

2.3 Results and Discussion

2.3.1 Synthetic Pore and Pore-Throat Size Distributions

2.3.1.1 Left-skewed

The synthetic left-skewed pore and pore-throat size distributions are shown in Figure 1B. Samples with these distributions are dominated by large pores and pore-throats. The corresponding mean of the pore and pore-throat size distributions are 35.89 µm and 34.70 µm, respectively. By comparison, the means for the 3w4 pore and pore-throat size distributions are smaller, 28.02 µm and 15.92 µm, respectively, reflective of the left-skewed characteristics of the synthetic distribution. The standard deviations of left-skewed pore and pore-throat distribution are +/- 9.22 µm and +/- 10.37 µm of the respective mean. Both values are less than the 3w4 sample standard deviations (+/- 14.23 µm and 12.61 µm, respectively), due to a smaller spread of pore and pore-throat sizes. The respective pore and pore-throat size distribution minimum values are held constant with the 3w4 sample, 4.94 µm and 2.25 µm respectively. The maximum values for the synthetic pore and pore-throat size distribution differ from the 3w4 sample where values are truncated at 50 µm such that the simulated unreacted porosity and permeability values are consistent with those of sample 3w4.

2.3.1.2 Normal

The synthetic normal pore and pore-throat size distributions are shown in Figure 1C. In these distributions, the average pore and pore-throat sizes are 30.69 µm and 19.52 µm, respectively. Both values are larger than the respective means of sample 3w4 (28.02 µm and 15.92 µm) given the higher frequency of large pores and pore-throats and lower frequency of small pores and pore-throats (Figure 1C). The standard deviation of the distributions' pore and pore-throat sizes are +/-

10.42 µm and +/- 10.75 µm of their respective mean, larger than those for sample 3w4. The minimum and maximum radii values here match those for sample 3w4.

2.3.1.3 Uniform

The synthetic uniform pore and pore-throat size distributions are shown in Figure 1D. Here, there is a uniform frequency for all pores and pore-throats such that all pore and pore-throat sizes have equal probability. The mean pore and pore-throat sizes are 27.45 µm and 26.15µm, respectively. The minimum pore and pore-throat sizes are set equal to those for 3w4 while the maximum pore and pore-throat values are set to 50 µm such that simulated unaltered porosity and permeability values agree. The standard deviation from the mean of the pore and pore-throat distributions are +/-13.05 µm and +/-13.83 µm. Here, the means and standard deviations are similar to those for sample 3w4 for both the pore and pore-throats size distributions.

2.3.2 Simulated Unreacted Porosity-Permeability

Simulated porosity and permeability for unaltered pore network modeling simulations, those using pore network models populated with the pore and pore-throat size distributions in Figure 1, are shown in Figure 2. As evident in Figure 2, the simulated initial porosity for pore network models created with each of the synthetic distributions agrees relatively well with the initial porosity for sample 3w4 (Figure 2A). The average simulated initial porosity for sample 3w4 is 0.13 in comparison with the simulated porosity for the left-skewed distribution of 0.19, 0.15 for the uniform distribution, and 0.17 for the normal distribution. By contrast, the simulated initial permeabilities for the synthetic distributions are up to two orders-of-magnitude higher than the initial simulated permeability for sample 3w4. This is driven by the higher frequency of large pore-

throats in each of the synthetic distributions in comparison to sample 3w4. The simulated permeability for the synthetic normal distribution is the closest to the initial permeability of sample 3w4. This is not surprising given that the corresponding means of both pore and pore-throat size distributions agree relatively well and this distribution has a lower frequency of large pore-throats as compared to the uniform and left-skewed distributions.

2.3.3 Simulated Reactive Porosity-Permeability Evolution

2.3.3.1 Uniform Reaction, Size Relative

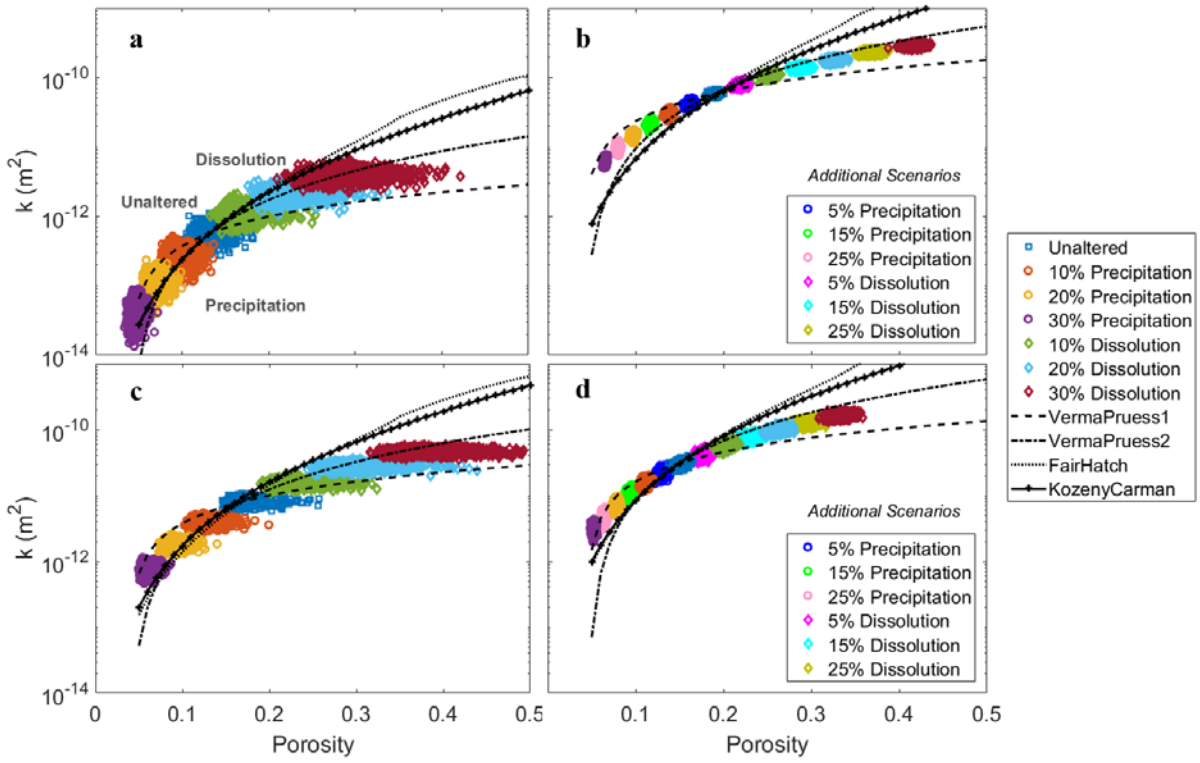

Figure 5: Simulated porosity and permeability given a uniform distribution of mineral dissolution and precipitation where reactions alter pore and pore-throat sizes by an amount relative to their unaltered size for pore network models populated using (a) 3w4 pore and pore-throat size distributions modified from Beckingham (2017); (b) synthetic left-skewed distributions; (c)

synthetic normal distributions; and (d) synthetic uniform distributions. Common macroscopic porosity-permeability relationships are shown (lines).

Simulated porosity-permeability for uniform reaction scenarios for the size-relative reaction extent are shown in Figure 5 for all three synthetic distributions in addition to simulation results for sample 3w4 from Beckingham (2017). These simulations reflect dissolution or precipitation occurring in all pores and pore-throats where the extent of reaction is related to the original pore and pore-throat sizes (e.g. 10% of the original pore or pore-throat size). As can be seen in Figure 5, the permeability increases with dissolution and decreases with mineral precipitation for all distributions. Qualitatively, there is little difference in the porosity-permeability evolution for all pore and pore-throat size distributions.

Differences in the spread of simulated porosities and permeabilities for reaction sub-scenarios are also evident in Figure 5. In general, a larger spread in simulated porosity occurs for dissolution scenarios and a smaller spread for precipitation. Furthermore, the spread in simulated porosity for dissolution sub-scenarios increases with reaction extents, where a larger spread is observed for dissolution by 30% of relative sizes versus 10%, for example. This is because the range of pore sizes increases with dissolution where a larger reaction extent results in a larger range of pore sizes. Similar, opposite, observations can be made for precipitation sub-scenarios where the spread of pore sizes is reduced with precipitation. The simulated reaction sub-scenario spreads are small for the left-skewed and uniform distributions in comparison with the other simulations. This is because the range of pore sizes for this distribution is much smaller than the other pore size distributions. Also, larger increases in porosity are observed for distributions with a larger fraction of large pores (e.g. left-skewed) in comparison to those with a smaller fraction of large pores (e.g. right-skewed).

Macroscopic porosity-permeability relationships are plotted as black lines in Figure 5 and depict an increase in porosity and permeability with dissolution and a decrease with precipitation. In comparison with simulation results, these relationships agree relatively well and reflect the simulated trend of porosity and permeability. The mean absolute error ratio (MAER) is calculated here, shown as Equation 2.8, and used to determine the agreement between simulated porosity-permeability and values calculated from the macroscopic porosity-permeability relationships where the lowest MAER value corresponds to the best agreement.

Calculated MAER values are given in Table 1. The Kozeny-Carman relationship, overall, fits best with the 3w4, and Fair-Hatch relationship best fits all synthetic distributions, as visually apparent and as reflected in the MAER values. The VermaPruess1 and VermaPruess2 equations are less representative of all simulated results, as evident from relatively higher MAER values.

2.3.3.2 Uniform Reaction, Discrete

The simulated porosity-permeability for pore network models reflecting a uniform reaction condition where all pores and pore-throats are altered by a set reaction zone thickness (i.e. 1, 5, or 10 μm) are shown in Figure 6. As shown in Figure 6, permeability and porosity increase due to mineral dissolution and decrease due to mineral precipitation for all pore and pore-throat size distributions. In simulations for sample 3w4 (Figure 6A) precipitation of a 10 μm coating drastically reduces permeability as the critical porosity is approached and pore-throats are clogged. This phenomenon is not observed for the other pore and pore-throat size distributions due to a lower frequency of small pore-throats. The extent of porosity and permeability alteration from the unaltered values increases as the reaction zone thickness increases, where a decrease in porosity

of ~30% is observed for a 5 µm precipitate coating versus a 50% porosity reduction for the 10 µm precipitate coating.

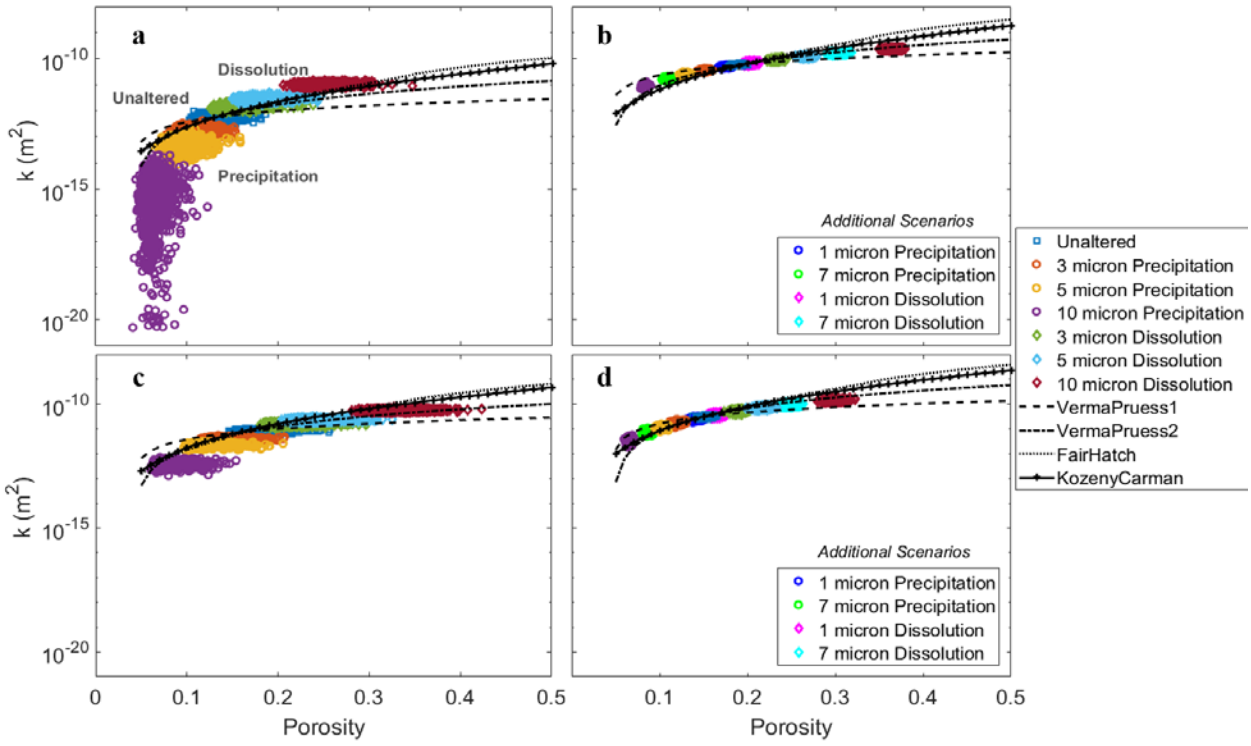

Figure 6: Simulated porosity and permeability for uniform reactions where pore and pore-throat sizes are altered to reflect dissolution and precipitation by increasing or decreasing sizes by a discrete value and compared with common porosity-permeability relationships (lines). Pore network models are populated using (a) 3w4 pore and pore-throat size distributions modified from Beckingham (2017), (b) synthetic left-skewed distributions, (c) synthetic normal distributions, and (d) synthetic uniform distributions.

Aside from the clogging observed for large precipitate coatings for sample 3w4, simulated porosity-permeability are qualitatively similar for all pore and pore-throat size distributions. However, porosity in dissolution reactions increases considerably more in synthetic left-skewed and synthetic uniform distributions due to the higher proportion of large pore-throats. The largest

decreases in simulated permeability due to precipitation reactions are observed for sample 3w4 and the normal distribution. These samples have proportionally a larger amount of small pore-throats. Similar observations regarding the spread in simulated porosity values, reflecting the range of pore sizes, are also observed here where simulated porosities for the left-skewed and uniform distributions have the smallest variation by visual inspection.

The macroscopic porosity-permeability relationships are shown in Figure 6 as black lines and agree relatively well with the simulated porosity-permeability for the synthetic pore and pore-throat size distributions. These relationships, however, deviate considerably from the simulated porosity and permeability for the 3w4 distribution as they are unable to reflect the large reduction in permeability due to pore-throat clogging. The VermaPruess2 relationship correlates with the lowest MAER values (Table 1) for 3w4, while all synthetic distributions correlate lowest MAER values with the Fair-Hatch relationship.

2.3.3.3 Random Reaction

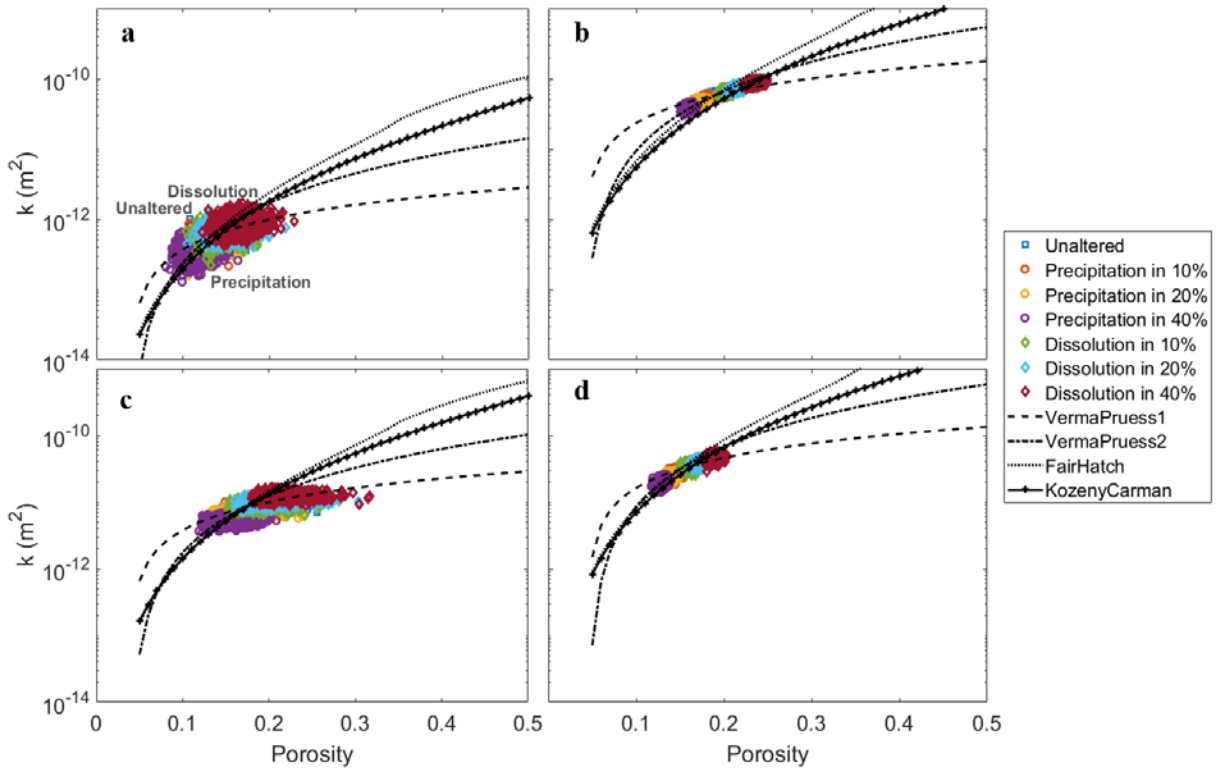

Figure 7: Simulated porosity and permeability evolution for randomly distributed mineral reactions occurring in 10-40% of all pores and pore-throats where radii are increased or decreased by 20% of their original size. Shown, are simulation results for pore network models populated with (a) 3w4 pore and pore-throat size distributions modified from Beckingham (2017), (b) synthetic left-skewed distributions, (c) synthetic normal distributions, and (d) synthetic uniform distributions. Also shown are common porosity-permeability relationships (lines).

Simulated porosity-permeability for the random reaction scenario is shown in Figure 7. Here, simulations are carried out to consider dissolution and precipitation reactions that occur randomly throughout 10, 20 or 40% of the matrix where pore and pore-throat sizes increase or decrease by 20% of their original sizes. As can be seen, permeability generally increases as porosity increases, regardless of pore and pore-throat size distribution. Relative to the other reaction scenarios, these reactions do not significantly alter porosity and permeability. This is

because these simulations correspond to a relatively small reactive volume where less than 50% of all pores and pore-throats are reacted.

Simulated porosity-permeability evolution for pore network models populated with each pore and pore-throat size distribution are qualitatively similar. As with the other reaction scenarios, distributions with larger proportions of large pores and pore-throats have larger increases in porosity and permeability for dissolution scenarios. A similar observation can be made for small pores and pore-throats for precipitation scenarios where larger reductions in permeability are evident for simulations using these distributions. Observed changes in the spread of simulated porosities, as discussed for the uniform reaction scenarios, can be made and apply here as well, where the smallest spread in sub-scenario simulations occurs for the left-skewed distribution.

Macroscopic porosity-permeability relationships (shown as lines in Figure 7) agree relatively well with the simulated porosity-permeability evolution. According to the MAER analysis (Table 1), the Kozeny-Carman and Fair-Hatch macroscopic relationships are the least representative of the simulated porosity-permeability evolution, also evident by visual inspection. Overall, The VermaPruess2 relationship better represents the simulations for all distributions.

2.3.3.4 Channelized Reaction

Simulated porosity-permeability evolution for channelized reaction scenarios, are shown in Figure 8. Here, all pores and pore-throats along a 3 x 3 x 10 centralized channel aligned with the flow direction are increased or decreased by 10% to 50% of their initial sizes. This results in small increases in porosity and permeability due to dissolution and small decreases in porosity and permeability due to precipitation. Simulations using pore and pore-throat size distributions for sample 3w4 and all synthetic distributions are qualitatively similar, where an obvious smaller

spread in simulated porosity is evident for simulations using the left-skewed and uniform distributions.

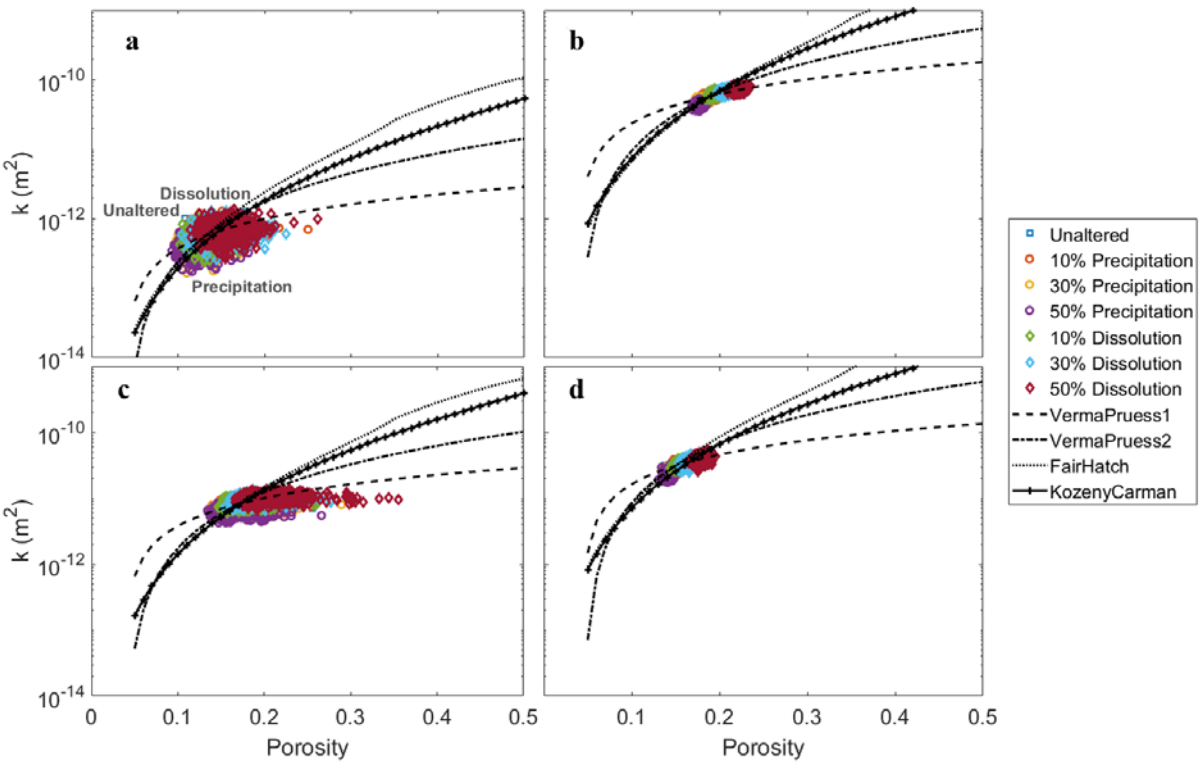

Figure 8: Simulated porosity and permeability for reaction occurring along a centralized 3 x 3 x 10 channel aligned with flow where pore and pore-throat radii are increased or decreased by 10 to 50% of their original size. Shown, are simulations for pore network models populated using (a) 3w4 modified from Beckingham (2017), (b) synthetic left-skewed, (c) synthetic normal and (d) synthetic uniform distributions. Also shown are common porosity-permeability relationships (lines).

The simulated porosity and permeability here appear similar to simulation results for the random reaction conditions (Figure 7). In the channelized scenario, approximately 10% of the

sample is impacted by dissolution or precipitation reactions. Given that the impacted pores and pore-throats are randomly sampled from the pore and pore-throat size distributions, this is equivalent to reactions occurring in ~10% of randomly selected pores and pore-throats, as simulated in the random reaction scenario.

The macroscopic porosity-permeability relationships, shown as black lines in Figure 8, agree relatively well with the simulated porosity-permeability evolutions. In particular, the VermaPruess2 relationship reflects the simulated permeability evolution for all pore and pore-throat size distributions and has the lowest MAER values (Table 1). All other macroscopic relationships are observed to slightly overestimate simulated permeability for dissolution and underestimate simulated permeability for precipitation scenarios.

Table 1: Mean absolute error ratios for simulated porosity-permeability for uniform, random and channelized reaction scenarios as compared to common macroscopic porosity-permeability relationships.

Distribution	Scenario	MAER Values			
		Kozeny-Carman	Fair-Hatch	Verma-Pruess1	Verma-Pruess2
Right-skewed	Uniform reaction, size-relative reaction	7.97E-05	9.59E-05	8.15E-05	8.52E-05
	Uniform reaction, discrete reaction thickness	4.08	3.86	9.30	3.15
	Random reaction	5.92E-05	5.76E-05	5.39E-05	4.58E-05
	Channel localized	5.74E-05	5.65E-05	5.16E-05	4.30E-05
Left-skewed	Uniform reaction, size-relative reaction	7.98E-05	7.84E-05	8.19E-05	8.14E-05
	Uniform reaction, discrete reaction thickness	9.63E-05	9.53E-05	9.83E-05	9.76E-05
	Random reaction	2.45E-05	3.37E-05	2.24E-05	1.93E-05
	Channel localized	2.12E-05	3.27E-05	2.63E-05	1.79E-05
Normal	Uniform reaction, size-relative reaction	1.29E-04	1.24E-04	1.49E-04	1.45E-04
	Uniform reaction, discrete reaction thickness	1.28E-04	1.24E-04	1.33E-04	1.36E-04
	Random reaction	2.75E-05	3.51E-05	2.25E-05	2.34E-05
	Channel localized	2.58E-05	3.38E-05	2.61E-05	2.00E-05
Uniform	Uniform reaction, size-relative reaction	8.03E-05	7.97E-05	8.15E-05	8.13E-05
	Uniform reaction, discrete reaction thickness	9.67E-05	9.63E-05	9.75E-05	9.74E-05
	Random reaction	1.62E-04	1.61E-04	1.63E-04	1.62E-04
	Channel localized	1.62E-04	1.61E-04	1.63E-04	1.62E-04

2.3.3.5 Size-Dependent Reactions, Small Pores and Pore-Throats

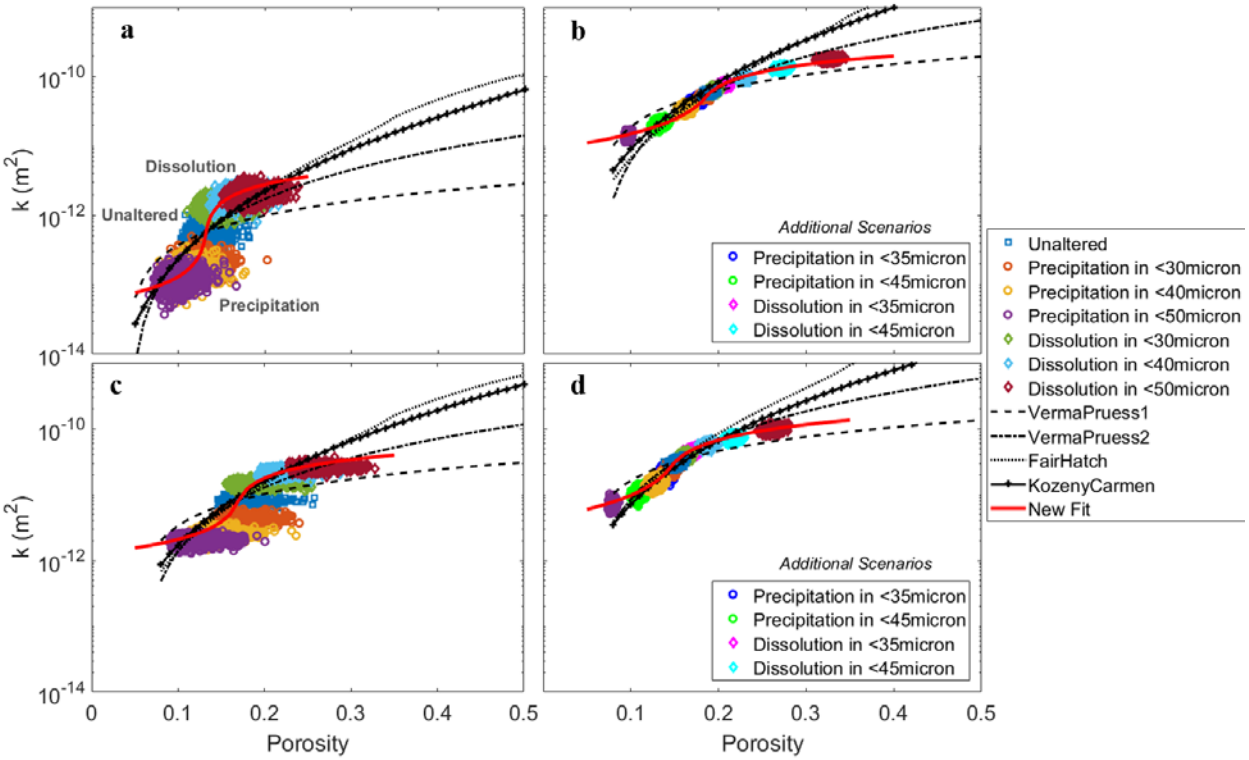

Figure 9: Simulated porosity-permeability for reactions initiating in small pores and pore-throats, where reactions alter radii by 20% of their initial value, and comparison to common porosity-permeability relationships (black lines) and modified Verma-Pruess relationship (red line). Shown, are results for pore network models populated with (a) 3w4, modified from Beckingham (2017), (b) synthetic left-skewed, (c) synthetic normal, and (d) synthetic uniform pore and pore-throat size distributions.

Simulations for reactions initiating in small pores and pore-throats are shown in Figure 9. In these simulations, the extent of reaction is relative to the pore or pore-throat's initial size and a reaction extent of 20% is evaluated. As evident in Figure 9, this results in a complex evolution of porosity and permeability. In general, porosity and permeability increase with dissolution and decrease with precipitation and simulations are overall qualitatively similar. For dissolution and precipitation, there are two distinct regions where the first reflects reactions in the smallest pores

and pore-throats and correspondingly small changes in porosity with larger changes in permeability. As reactions progress to larger pores and pore-throats, porosity and permeability changes are more equivalent. This phenomenon is most evident in simulations for sample 3w4 which has the largest relative proportion of small pores and pore-throats and least evident in simulations for the left-skewed and uniform distributions which have the smallest relative proportion of small pores and pore-throats.

Common macroscopic relationships are shown as black lines in Figure 9. These relationships are unable to reflect the observed phenomenological porosity-permeability evolution. To reflect these phenomena, a modified Verma-Pruess porosity-permeability relationship is developed. The improved relationship is constructed as a step-function where the application is related to reaction type, precipitation or dissolution, and is given by,

$$K = \begin{cases} K_0 \left(\frac{\alpha \Phi_o}{(1+\alpha)\Phi_O - \Phi} \right)^{n_1} & for\ \Phi < \Phi_o \\ K_0 \left(\frac{\Phi - (1-\alpha)\Phi_0}{\alpha \Phi_O} \right)^{n_2} & for\ \Phi > \Phi_o \end{cases} \qquad (2.9)$$

where K_O is initial permeability, Φ_O is initial porosity, Φ is simulated porosity, α is a fitting parameter, and n_1 and n_2 are empirical power law exponents. Optimized parameters for α and n, those that result in the minimum MAER values, are given in Table 2 for each pore and pore-throat size distribution. The corresponding MAER values for this new relationship, and all other relationships, are given in Table 3. Overall, the improved macroscopic relationship better fits the simulated porosity-permeability as indicated qualitatively in Figure 9 and quantitatively, for some simulations, by MAER error analysis. For simulations using the synthetic left-skewed distributions, MAER values of the improved relationship are lower than the other macroscopic porosity-permeability relationships (Table 3). MAER values for the synthetic normal and uniform

pore and pore-throat size distributions, however, are not quantitatively the best fit but are able to qualitatively reflect the non-linear evolution of permeability.

Table 2: Optimized fitting parameters for precipitation and dissolution reactions for the modified Verma-Preuss relationship for size dependent reactions.

	Improved Fit Parameters for Reactions Initiated in Small Pores and Pore-throats				**Improved Fit Parameters for Reactions Initiated in Large Pores and Pore-throats**			
	Precipitation ($\Phi < \Phi_0$)		Dissolution ($\Phi > \Phi_0$)		Precipitation ($\Phi < \Phi_0$)		Dissolution ($\Phi > \Phi_0$)	
	α	n	α	n	Φ_c	n	Φ_{cc}	n
3w4 Sample	0.02	0.5	0.02	0.6	0.05	0.9	0.345	0.9
Synthetic Left-skewed	0.1	0.5	0.1	0.8	0.072	0.9	0.379	0.9
Synthetic Normal	0.04	0.5	0.04	0.6	0.064	0.9	0.434	0.9
Synthetic Uniform	0.12	0.6	0.12	0.9	0.06	0.9	0.308	0.9

2.3.3.6 Size-Dependent Reactions, Large Pores and Pore-Throats

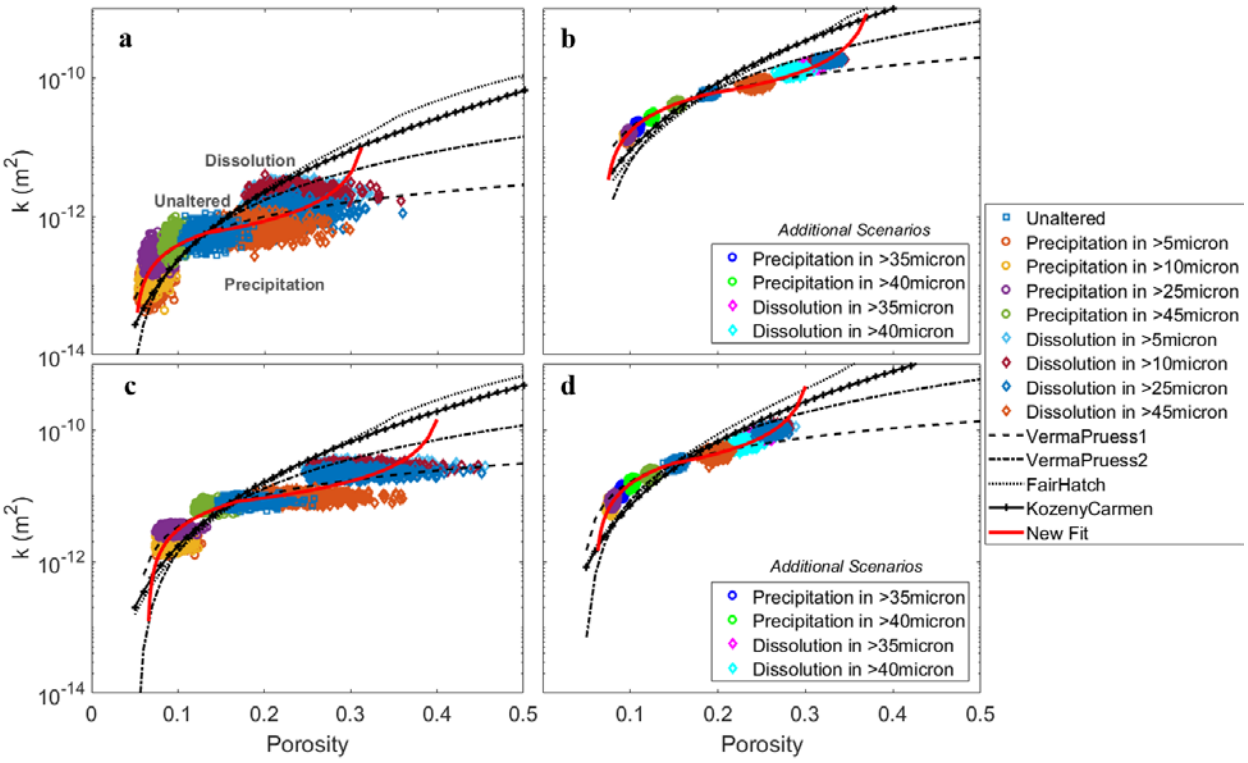

Figure 10: Pore network model simulated porosity-permeability evolution for reactions initiating in large pores and pore-throats and altered by 20% of their initial size. Simulations are shown for models populated with (a) 3w4, modified from Beckingham (2017), (b) synthetic left-skewed, (c) synthetic normal, and (d) synthetic uniform pore and pore-throat size distributions. Common macroscopic porosity-permeability relationships (black lines) and modified Verma-Pruess relationship (red line).

Simulated porosity-permeability for dissolution and precipitation reactions that initiate in large pores and pore-throats are shown in Figure 10. In this scenario, reactions occur in pore and pore-throats larger than a given radii (e.g. 5, 10, 25, and 50 µm) and occur in pores and pore-throats with smaller radii as the reaction progresses. When reactions occur only in the largest pores and pore-throats, porosity increases or decreases with little change in permeability. As reactions

proceed to smaller pores and pore-throats, increases or decreases in porosity and permeability occur with dissolution or precipitation, respectively. This non-uniform phenomena is observed in all simulations but is the least prevalent in simulations using the left-skewed and uniform distributions. These distributions have a high frequency of large pores and pore-throats such that reactions occur in the majority of pore-throats initially resulting in an earlier change in permeability compared to other simulations. The spread in simulated porosity-permeability increases as reactions progress for all pore and pore-throat size distributions, as observed in the other reaction scenarios.

Common macroscopic porosity-permeability relationships, shown as black lines in Figure 10, are unable to reflect the overall observed phenomena, often overestimating permeability in dissolution areas and underestimating permeability from precipitation reactions. However, the Verma-Pruess equation captures the precipitation regime relatively well. To better reflect the observed non-linear mechanisms of permeability evolution, a modified version of the Verma-Pruess relationship was created as a step-function. This modified version of the Verma-Pruess relationship uses the original Verma-Pruess function for the precipitation regime and a modified version for the dissolution regime and as given by,

$$K = \begin{cases} K_0 \left(\frac{\Phi - \Phi_c}{\Phi_0 - \Phi_c}\right)^n & for\ \Phi < \Phi_o \\ K_0 \left(\frac{\Phi_0 - \Phi_{cc}}{\Phi - \Phi_{cc}}\right)^n & for\ \Phi > \Phi_o \end{cases} \tag{2.10}$$

where K_0 is initial permeability, Φ_0 is initial porosity, Φ is simulated porosity, Φ_c is critical porosity where permeability approaches zero (~0.3 Φ_0) and Φ_{cc} is the critical porosity for consolidation above which the rock is no longer consolidated (typically 36-40% for sandstones) (Dvorkin and Nur 2002), and n is an empirical power law exponent. Optimized parameters for the improved fit are given in Table 2 with calculated MAER values given in Table 3. This relationship better fits

the simulated permeability evolution for each pore and pore-throat size distribution both visually (Figure 10) and as quantified by the lowest MAER (Table 3).

Table 3: MAER analysis for simulated porosity-permeability for dissolution and precipitation reactions initiating in small and large pores and pore-throats compared to macroscopic porosity-permeability relationships.

	MAER VALUES									
	Reactions initiated in large pores and pore-throats					***Reactions initiated in small pores and pore-throats***				
	3w4 Sample									
	KozCarm	FairHatch	VP1	VP2	Modified VP	KozCarm	FairHatch	VP1	VP2	Modified VP
Dissolution	1.14E-04	2.91E-04	7.08E-05	1.35E-04	7.07E-05	8.33E-05	8.25E-05	1.15E-04	9.05E-05	1.42E-04
Precipitation	1.24E-04	9.68E-05	7.58E-05	1.04E-04	6.82E-05	2.68E-04	2.63E-04	3.80E-04	2.71E-04	1.94E-04
	Synthetic Leftskewed Distribution									
	KozCarm	FairHatch	VP1	VP2	Modified VP	KozCarm	FairHatch	VP1	VP2	Modified VP
Dissolution	1.27E-04	1.94E-04	3.12E-05	4.83E-05	1.02E-05	5.56E-05	8.54E-05	2.85E-05	1.98E-05	1.05E-05
Precipitation	5.99E-05	6.48E-05	1.92E-05	6.55E-05	7.97E-06	2.49E-05	2.78E-05	3.87E-05	2.73E-05	1.73E-05
	Synthetic Normal Distribution									
	KozCarm	FairHatch	VP1	VP2	Modified VP	KozCarm	FairHatch	VP1	VP2	Modified VP
Dissolution	2.49E-04	3.98E-04	5.25E-05	1.14E-04	6.16E-05	6.80E-05	8.38E-05	8.76E-05	5.80E-05	7.62E-05
Precipitation	9.60E-05	9.95E-05	5.89E-05	1.03E-04	5.31E-05	1.53E-04	1.64E-04	2.47E-04	1.68E-04	3.29E-04
	Synthetic Uniform Distribution									
	KozCarm	FairHatch	VP1	VP2	Modified VP	KozCarm	FairHatch	VP1	VP2	Modified VP
Dissolution	1.27E-04	1.63E-04	3.08E-05	5.66E-05	1.26E-05	3.77E-05	7.01E-05	3.40E-05	2.17E-05	1.45E-05
Precipitation	5.31E-05	5.69E-05	2.88E-05	5.95E-05	1.19E-05	3.05E-05	3.51E-05	6.89E-05	4.11E-05	9.44E-05

2.4 Conclusions

In this work, pore network modeling is used to examine the impact of variations in pore and pore-throat size distributions on the evolution of porosity and permeability for uniform and non-uniform spatial distributions of reactions as well as variations of reaction extents. Previous simulations of a sandstone sample, considered here for comparison, revealed that large variations in the evolution of porosity and permeability occur for different spatial distributions of mineral reactions (Beckingham 2017). Similar pore network modeling simulations from this work using synthetic left-skewed, normal, and uniform pore and pore-throat size distributions resulted in similar

variations in porosity-permeability that depend on the spatial distribution of mineral reactions. These simulations revealed that variations in pore and pore-throat size distributions do not have a considerable impact on the qualitative nature of the simulated porosity-permeability evolution. However, quantitative differences are evident, largely resulting from the relative fraction of small or large pores and pore-throats.

Simple macroscopic porosity-permeability relationships are often used to predict the reactive evolution of permeability. These relationships are able to successfully reflect the evolution of permeability in some, but not all, reaction scenarios. In systems where reactions occur uniformly on all surfaces and do not result in pore-throat clogging, these macroscopic relationships work well regardless of the characteristics of the pore and pore-throat size distributions. They are also able to reflect the evolution of porosity-permeability when reactions occur in a fraction of pores and pore-throats of varying size, as with the random and channelized reaction scenarios. Commonly used macroscopic relationships are unable to capture the porosity-permeability evolution when reactions initiate in small or large pores. In these scenarios, porosity and permeability evolves in a complex manner where reactions initiating in small pores and pore-throats initially significantly impact permeability and reactions initiating in large pores and pore-throats initially largely impact porosity. Here, modified versions of the Verma-Pruess relationship are created, taking the form of a step-function with distinct functions for dissolution and precipitation. These modified relationships successfully reflect the observed phenomena for the size-dependent reaction scenarios. While evident qualitatively, the MAER for this improved fit does not always reflect the best fit with the simulated results, primarily in dissolution scenarios when pore and pore-throat size distributions have a high frequency of small pores. However, the existing commonly used macroscopic relationships clearly do not reflect the observed complex phenomena for the size-

dependent reaction scenarios, as evident by visual disparity when compared to simulated porosity-permeability

Chapter 3

Impact of reaction gradients on the evolution of reactive permeability

3.1 Introduction

As a means of reducing atmospheric CO_2 emissions, CO_2 can be injected into a deep saline aquifer and stored. Once injected, CO_2 dissolves into formation brine, lowering pH and creating conditions favorable for mineral dissolution and precipitation reactions as the plume migrates away from the well. Porosity generally increases with dissolution and decreases with precipitation. Nonetheless, porosity may evolve dynamically at the reservoir scale where dissolved minerals in the injection region may reprecipitate at some distance away from the well (Bacci et al., 2011a; Luquot and Gouze, 2009; Peuble et al., 2019) or sodium ions in near-well brine crystalize and precipitate (Bacci et al., 2011b; Jeddizahed and Rostami, 2016), although dissolution is most likely to occur in injection scenarios due to low pH and fluid saturation (Nogues et al., 2013). The impact of these propagated reactions on permeability is further complex and not well understood.

Constitutive properties of porous media, such as grain size and pore distribution, as well as reactive fluid composition, control the evolution of porosity and permeability by driving mineral reactions. An experimental in-situ imaging study in Menke et al. (2017), showed initial pore and pore-throat structure and brine acidity have considerable effects on porosity and permeability where a homogeneous pore sample and initial brine pH of 3.6 resulted in a 47% increase in porosity and a 3% increase in permeability. In Nogues et al. (2013) a series of reactive flow-through

experiments evaluated the influence of variations in flow-rate, pH, and pore-scale mixing effects on porosity and permeability resulting in transport-limited dissolution regimes, where high flow-rates and high concentrations of carbonic acid produced extensive permeability evolution. The transport and reactivity of a chemical species in a porous media can be quantified by the Péclet (Pe) and Damköhler (Da), where calculated values are the ratio of advection to diffusion in liquid-phase, and reaction rate to diffusive mass transfer in solid-phase, respectively. For large Pe and small Da scenarios, observed in Nunes et al. (2016), the system is reaction-limited, resulting in a uniform dissolution regime and a rapid increase in permeability. Conversely, in Mangane et al. (2013), the clogging of macro-pores at low pCO_2 concentrations resulted in a decrease in permeability, from approximately 40 mD to 8 mD, while a high pCO_2 scenario led to the development of preferential flow paths and an increase in permeability. In ”salting-out” conditions near wellbore during CO_2 injection, factors such as injection rate and brine salinity effect salt precipitation, while salt precipitation decreases with injection rate and increases with salinity and can greatly effect injectivity (Jeddizahed and Rostami, 2016). Nonetheless, these studies show that no single geochemical variable alone is a good indicator of porosity and permeability evolution (Garcia-Rios et al., 2015; Nogues et al., 2013).

Dissolution and precipitation reactions may migrate through a region as a uniform reactive front, resulting in a change in porosity and permeability. Numerical modeling simulations in Nogues et al. (2013) of reactive transport in porous media suggest dissolution regimes in diffusive-dominated systems causes localized reactions near the injection inlet, while systems dominated by advective transport experienced a uniform dissolution reaction regime. In Voltolini and Ajo-Franklin, (2019), an in-situ XCMT study of dissolution in a limestone sample resulted in a uniform dissolution front developing in early injection stages (i.e. initial 4 hours) when more reactive

material is available. Initial pore structures and influent fluid composition have also been observed to control dissolution regimes, as observed in a micro-CT imaging study in Menke et al. (2017), where homogenous pore-structures, such as the Ketton limestone, dissolved uniformly at relatively high pH (e.g. pH 3.6) (Menke et al., 2015; Menke et al., 2017). In near wellbore regions during injection, super-critical CO_2 streams may evaporate formation brine and precipitate salts, most efficiently when the brine has sufficient mobility through the network and precipitation front is continuously recharged (Bacci et al., 2011b). Although factors such as fluid salinity and injection rate may alter the reaction migration pattern (e.g. Jeddizahed and Rosami, 2016) near the wellbore as well as at a distance from the injection well.

Dissolution and precipitation reaction fronts may also result in a gradient in the extent of reaction as the front propagates. CO_2 is typically injected at high flow rates and migrates laterally, displacing and mixing with the residual formation fluid (Peuble et al., 2019). The CO_2 plume, as a less dense, less viscous super-critical state, also migrates upwards due to density differences (Singh et al., 2019; Zhang et al., 2017b). Near the injection well, high flow rates may drive heterogeneous geochemical reactions causing local heterogenous dissolution regimes where further away from well dissolution may become homogeneous (Egermann et al., 2005; Vialle et al., 2014). Variations in dissolution front is also observed in an ex-situ X-ray micro-CT experimental study where dissolution is more abundant near the injection region and decreases along the sample length (Qajar and Arns, 2016). Assuming a change in porosity is proportional to the extent of a dissolution regime, one may expect porosity to follow similar trends. For example, experimental reactive flow-through studies of a bioclastic limestone (e.g. Vialle et al.,2014), showed an increase of inlet porosity from 0.28 to 0.36, while outlet porosity was constant with little variation, suggesting a decrease in the extent of dissolution over the length of the sample.

This is further analyzed in Mangane et al. (2013), where the clogging of macropores by fine migration was observed to occur over short distances due to the decrease of fluid dissolution capacity. Similarly, a series of four flow-through experiments in Luquot and Gouze (2009) represented near-well injection regions and distant locations from well where dissolution is uniform, possibly resulting in a reaction extent gradient over the length of the reservoir, where high rates of dissolution occur near the inlet and less structural modification at a given distance. Numerical models of CO_2 injectivity in a deep saline aquifer given a non-uniform reaction scenario also suggested that numerous wormholes at inlet converge to a single flow path at outlet resulting in a permeability drop from 2 mD to approximately 1 mD (Bacci et al., 2011a).

In this study, the evolution of porosity and permeability in various transport and reaction-limited regimes is investigated using pore network model simulations. Here, the migration of a reactive front through a pore network that results in a uniform distribution of reactions as the front migrates through the network is simulated reflecting conditions with Da values less than 1, regardless of Pe value (e.g. Soulaine et al., 2018). Simulations reflecting flow regimes that result in a gradient of reaction extents in the direction of fluid flow is also simulated, reflecting Da values greater than 1 and considerable small Pe value (e.g. $< 10^{-2}$) conditions. Simulation results are compared to each other and with macroscopic porosity-permeability relationships.

3.2. Materials and Methods

3.2.1. Alberta sandstone basin sample

Topographic data (e.g. pore and pore-throat size distributions) of a Viking sandstone sample, termed as “3w4”, is considered here. This sample has been studies in previous literature works, where Kim et al. (2011) and Beckingham et al. (2013) determined pore and pore-throat size

distributions, and Peters (2009) analyzed sample composition. This sample is composed of quartz (73 +/- 3%) with 21 +/- 2% Mg chlorite, kaolinite, montmorillonite and albite, as determined by SEM in Peters (2009). The porosity of sample 3w4 is 14-18% as determined from SEM and X-ray CT imaging analysis in Peters (2009) and Kim et al. (2011). Initial permeability ranges from 2.4 x 10^{-13} to 4.5 x 10^{-13} m^2, determined in Beckingham et al. (2013) by probe permeameter. The topographic data of sample 3w4 were determined by 3D X-ray CT imaging using 3DMA-Rock in Kim et al. (2011) where Figure __ shows the pore and pore-throat size distribution of the 3w4 sample. The mean and standard deviation of the pore sizes are 28.02 μm and 14.23 μm, respectively, where pore-throat sizes have a mean and standard deviation of 15.92 μm and 12.62 μm, respectively. The minimum and maximum pore sizes are 4.94 and 235.83, respectively, and 2.25 and 137.31 for pore-throat sizes, respectively.

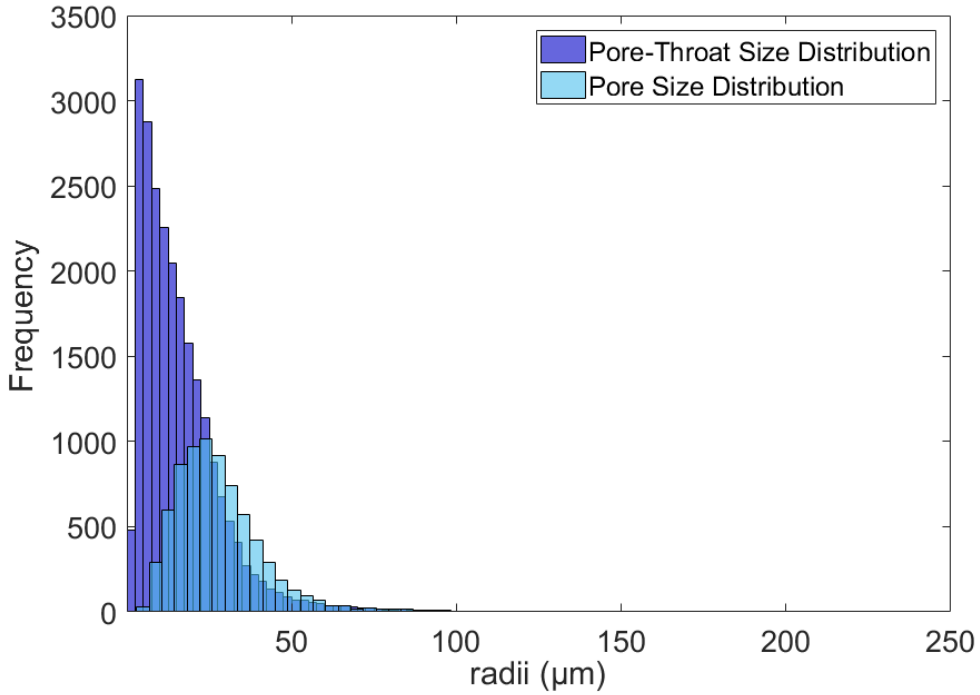

Figure 11: Pore and pore-throat size distributions from sample "3w4" used to populate the pore network model

3.2.2. Pore Network Modeling

Following the work of Beckingham (2017) as well as discussed in chapter 2, pore network modeling was used here to simulate reactive permeability where simulations build on the pore network model developed in Li et al. (2007) and Beckingham et al. (2013). The pore network is constructed as a 10 x 10 x 10 grid containing a total of 1000 nodes (e.g. pores) and defined on a regular, cubic lattice of which was validated in Arns et al. (2004). Pores were connected by pore-throats and represented as idealized smooth spheres. Pore-throats were represented as smooth cylinders. Both pore and pore-throat radii were randomly sampled from the pore and pore-throat size distributions obtained in Kim et al. (2011) and shown in Figure 11. Here a maximum of 26 connections was allowed for each pore, after the model proposed by Raoof and Hassanizadah

(2009), where pore coordination depends on pore size with a minimum of 2 connections and a maximum of 26 which followed the coordination number-pore size relationship for sample 3w4 determined in Kim et al (2011). An applied pressure differential drove flow across the entire pore network where permeability, *K*, was estimated from Darcy's law as given by,

$$K = \frac{Q_T v L}{\Delta P \Lambda} \tag{3.1}$$

where Q_T is the total flow rate through the network which was determined by summing flow from pore-throats at outlet, Λ is the cross-sectional area of the network, *v* is the fluid viscosity, *L* is the network length, and ΔP is the applied pressure differential between the inlet and outlet (e.g. Li et al., 2007). The flow between two connected pores was given by,

$$Q_{ij} = C_{ij}(P_i - P_j) \tag{3.2}$$

where C_{ij}, is the conductance of the pore-throat connecting pore *i* to pore *j* and P_i and P_j is the pressure in pores *i* and *j*, respectively (Li et al. 2007). The conductance, $C_{ij,}$ was given by Hagen-Pouseuille's law for incompressible fluid flow

$$\mathrm{C_{ij}} = \frac{\pi d_{ij}^4}{128 v l} \tag{3.3}$$

where d_{ij} is the diameter of the pore-throat connecting pore *i* pore *j*, *v* is viscosity, and *l* is the pore-throat length after Li et al. (2007). This pore network model was validated in Beckingham et al. (2013) where simulated permeability for the 3w4 sandstone sample agreed with experimentally measured values. This model was also used to simulate reactive permeability evolution for sandstone 3w4 in Beckingham (2017) and three synthetic distributions in Chapter 2, where similar simulations were carried out in this work to study effect of dissolution and precipitation reactive front propagation.

3.2.3. Dissolution and Precipitation Reaction Front Migration

Uniform mineral dissolution and precipitation reactions that propagate due to the migration of the reactive front through a pore network are considered here. In chapter 2, reactions occurred throughout the entire 10 x 10 x 10 network domain, varying by extent and spatial distribution. In each simulation sub-scenario considered here, the reactive front, and corresponding location of mineral dissolution or precipitation reactions, migrate away from the origin (e.g. injection well) and the porosity and permeability is simulated. For each sub-scenario that corresponds to an increase in the distance of the front location from two to ten units from the origin, 1000 simulations are run.

3.2.3.1. Uniform Front Migration

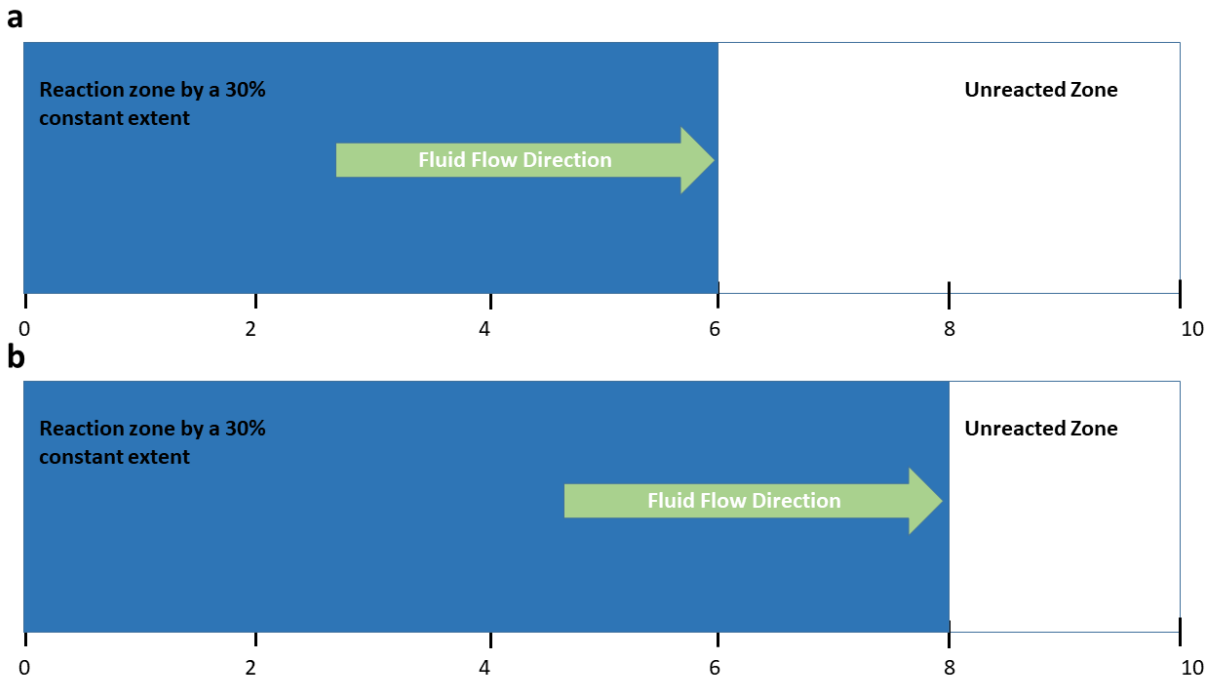

Figure 12: Uniform reaction front migration schematic resembling pore network model simulation scenarios. Here, the reactive front migrates from the origin to the outlet with a constant reaction extent. An example is shown for migration from (a) location 6 to (b) location 8. Pore and pore-throats in the unreacted zone have not been altered.

Uniform dissolution and precipitation reactions have been observed in previous works (e.g. Crandell et al., 2012; Qajar and Arns, 2016) where factors such as flow-rate and fluid composition affect plume formation and migration away from injection well (e.g. Nogues et al., 2013; Singh et al., 2019). In some cases, these reaction fronts propagate through the network by a uniform extent, altering porosity and permeability by increasing or decreasing pore and pore-throat sizes. Here, a constant reaction extent that increases (dissolution) or decreases (precipitation) pore or pore-throat radii by 30% of their unaltered values migrating through the network is considered. This may represent a core flood experiment or field system with a constant supply of reactive fluid pumped through the system, for example. As the front migrates, the pores and pore-throats in the given cross section of the network perpendicular to flow are either increased or decreased by 30%, representing dissolution and precipitation, respectively. For example, at a reactive front location of six, the sizes of all pores and pore throats between the origin and location six will be altered by 30%. At reactive front location ten, the entire network participates in the reaction such that the observed porosity and permeability matches that obtained for the uniform size relative reaction scenario considering a reaction extent of 30%, as shown in Chapter 2, Figure 5.

3.2.3.2. Gradient Front Migration

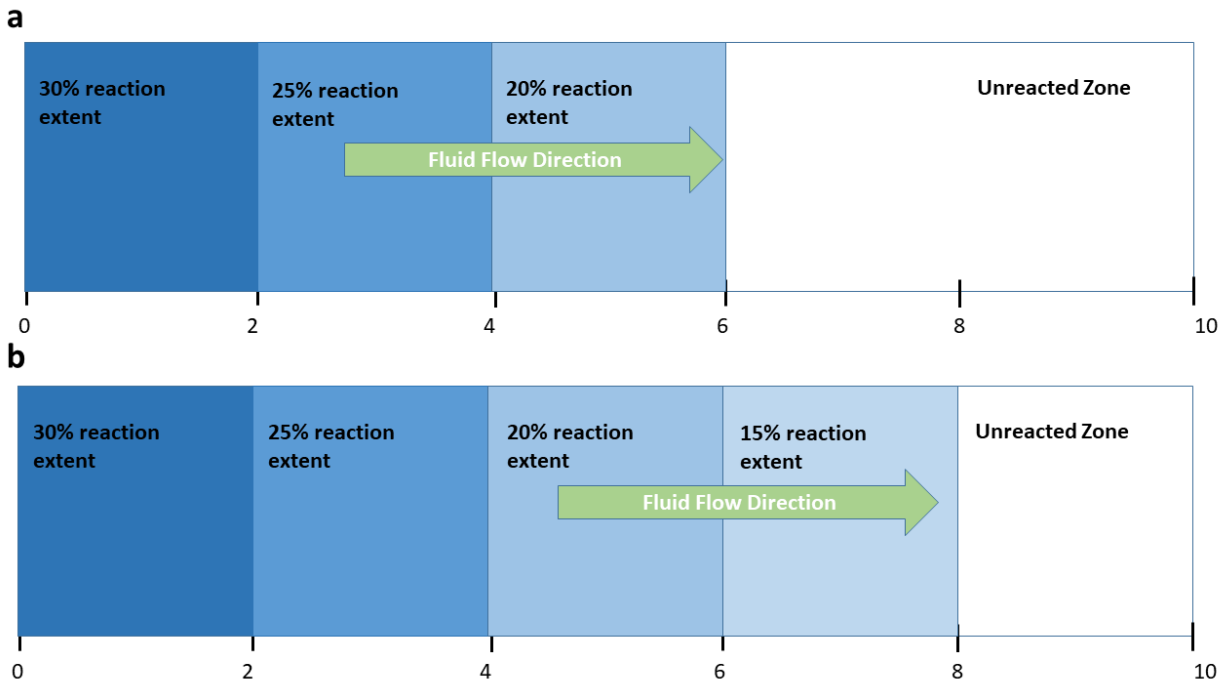

Figure 13: Gradient reaction front schematic utilized in pore network model simulations. Here, the reactive front migrates from the origin to the outlet, decreasing the reaction extent at each slice location. An example is shown for migration from (a) location 6 to (b) location 8. The unreacted zone is the region where pore and pore-throat sizes have not been altered.

In some experimental reactive flow-through studies, the reaction extents have been observed to decrease as the distance from the injection well (e.g. origin) or inlet increases (e.g. Mangane et al., 2013). For this scenario, a decrease in reaction extent by 5% increments at four locations along the domain length is considered. For example, in the domain closest to the origin (e.g. locations from zero to two) an extent of 30% is considered, at x-locations two to four the extent is 25%, from four to six the extent is 20%, and the trend is continued until the outlet is reached at location 10. When the reactive front reaches the outlet, the reaction gradient is complete where reactions vary from 30% to 10% reaction extents relative to original pore or pore-throat sizes.

3.3 Results and Discussion

3.3.1. Simulated Porosity Evolution for Migrating Uniform and Gradient Reaction Fronts

Pore network model simulated porosity evolution for dissolution and precipitation reactions considering migration of the reactive front through the network are shown in Figure 14 for those that result in a uniform and gradient extent of reactions throughout the network. These simulations reflect the change in porosity as the reactive front progresses through a sample, beginning at an inlet (e.g. origin) and ending at the outlet (e.g. x location 10). The porosity values here have been normalized by the unaltered porosity of the sample averaged over 1000 simulations, where the

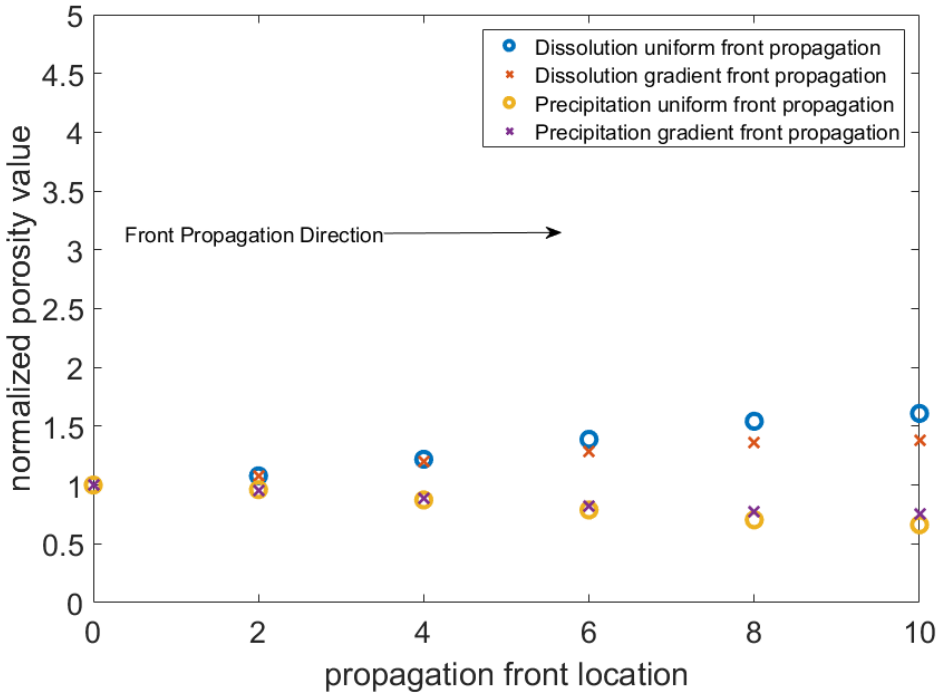

Figure 14: Simulated porosity averaged over 1000 simulations and normalized by unaltered porosity value given a uniform reaction scenario where pore and pore-throats are altered by some amount relative to their unaltered size. Simulations consider migration of a uniform front or a gradient reaction front.

unaltered porosity value is 0.133. As can be seen in Figure 14, the dissolution front increases porosity, while precipitation decreases porosity over the distance of the network.

Differences in the evolution of the dissolution and precipitation reactions as they propagate through the network are evident in in Figure 14. The change in porosity is greater due for dissolution reactions than precipitation reactions, where porosity at the furthest location (e.g. x location 10) is increased by 50% of its initial value due to dissolution and reduced by 30% due to precipitation.

The change in porosity is also dependent on the extent of reactions as the front migrates. Differences are observed for the uniform front and gradient front migration simulations, where reactions migrating at a uniform extent drive larger changes in porosity than gradient front scenarios at a given front location. This deviation is first evident at a front location of 6, where the reactive region is greater than half of the network. For the precipitation reaction front, the deviation between the uniform and gradient scenarios is not as evident and less change in porosity is observed.

3.3.2. Simulated Permeability Evolution with Migrating Reaction Fronts

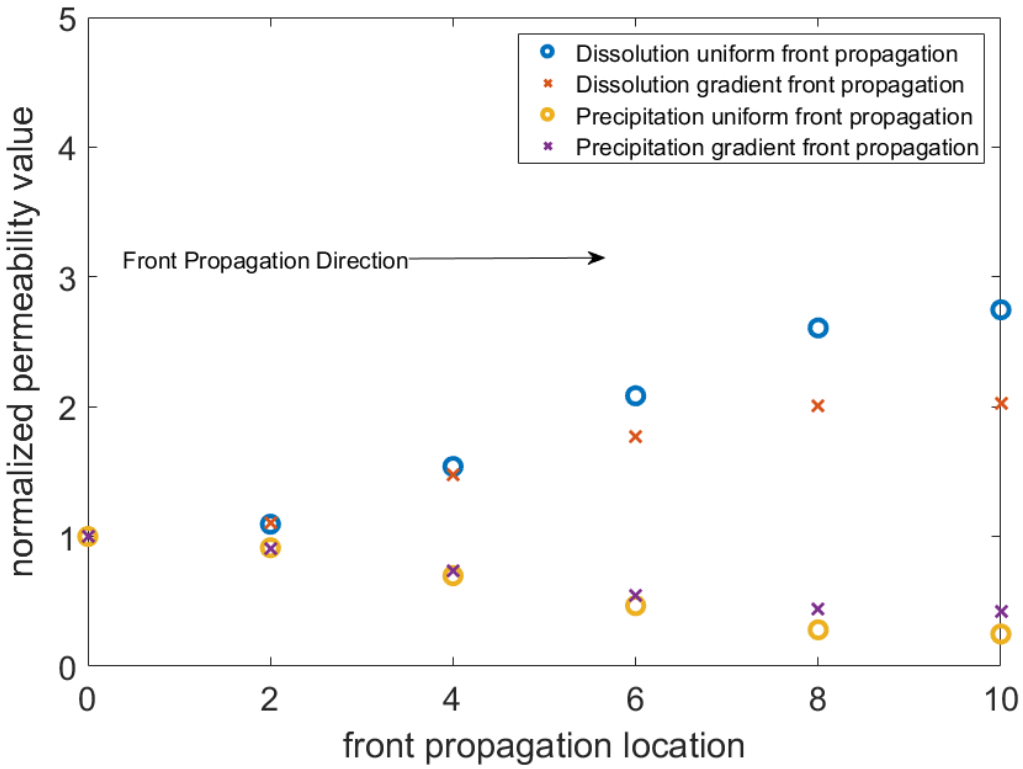

Figure 15: Simulated permeability averaged over 1000 simulations and normalized by the unaltered permeability given a uniform reaction scenario where pore and pore-throats are altered by some amount relative to their unaltered size. Dissolution and precipitation reaction migration along a sample are plotted where reaction fronts propagate uniformly or by a gradient.

Simulated permeability evolution for the migrating dissolution and precipitation fronts for both a uniform reaction front and gradient front in sample 3w4 are shown in Figure 15. Similar to Figure 14, these simulations reflect the change in permeability as the reactive front migrates through the network, beginning at the inlet (x location 0) and continuing to the outlet (x location 10). Results depict the normalized permeability as computed as a ratio of the simulated value over the unaltered

permeability of 5.7×10^{-13} m^2. As can be seen in Figure 15, the dissolution reaction front increases permeability, while precipitation decreases permeability over the distance of the network, similar to porosity evolution.

It is evident that the dissolution reaction front results in a greater change in permeability than does precipitation, where the permeability has at the least doubled from its unaltered values as a result of the dissolution front. Nonetheless, the change in permeability for the dissolution and precipitation reaction fronts are greater than the observed change for porosity (e.g. Figure 14). For precipitation, the decrease from the unaltered permeability value is approximately 0.8, which is considerably greater than the respective change observed for porosity. Small pore-throats control permeability and large pores control porosity, such that the greater change in permeability can be linked to the large frequency of small pores and pore-throats, shown in Figure 11.

The simulated permeability evolution depends on if the reaction front results in uniform extents or a gradient of reaction extents in the network, as also seen for simulated porosity evolution. However, the deviations here are much greater for both dissolution and precipitation reaction regimes. For dissolution, the deviation reaches a maximum at a front location 10, with a difference of around 0.72 between the uniform and gradient fronts, where for precipitation the difference of normalized permeability at location 10 is 0.17. Permeability evolution when reactions occur to a uniform extent results in a larger change than for reactions propagating with a gradient extent. This observation is similar to the observed evolution in porosity.

3.3.3. Simulated Reactive Porosity-Permeability Evolution

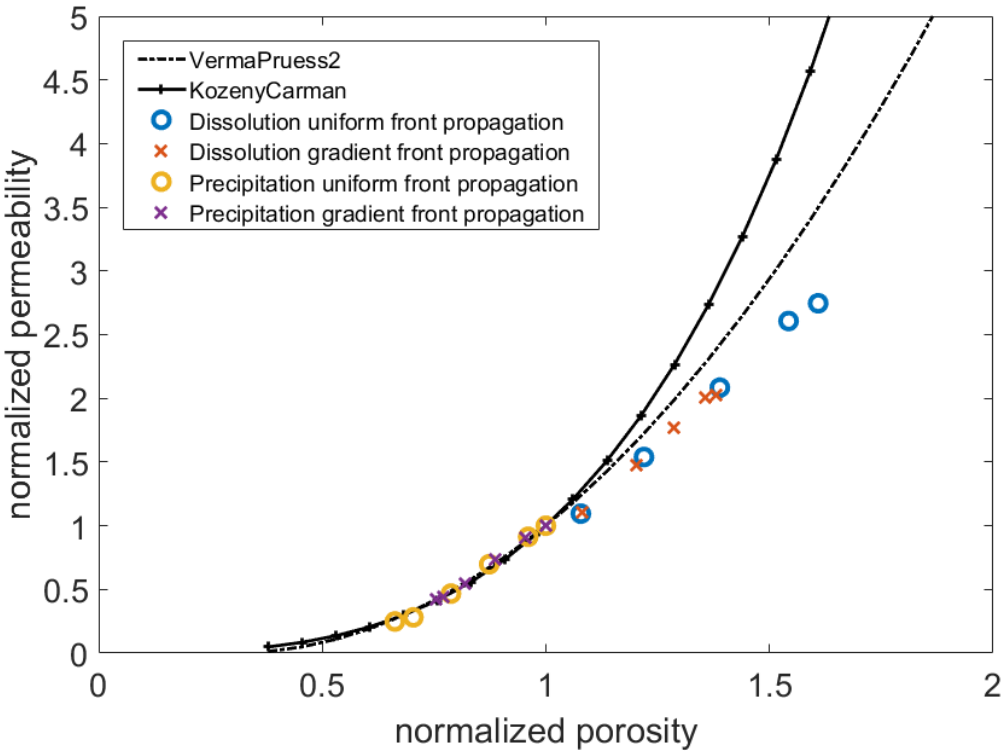

Figure 16 : Simulated porosity and permeability averaged for 1000 simulations and normalized by unaltered sample porosity and permeability, given a reaction scenario where pore and pore-throat sizes are altered uniformly by 30% relative to their unaltered size. Reactions are propagated through network either by a uniform reactive front or a gradient front. Common macroscopic porosity-permeability relationships are shown (black lines) for comparison to simulated data.

Simulated porosity-permeability evolution for the migrating reaction front is shown in Figure 16 for sample 3w4. Here, the migration of the reaction front results in a uniform extent of reactions or a gradient in the extent of reaction. Simulation results are compared to two commonly used macroscopic porosity-permeability relationships, the Kozeny-Carman and Verma-Pruess

equations, shown as black lines. Simulated porosity and permeability values at each x location are averaged over 1000 simulations and normalized by their unaltered values, 0.133 and 5.7 x 10^{-13} m^2, respectively. Here, permeability increases with porosity with a greater change in fronts that result in a uniform extent of reaction compared to those that result in a gradient in reaction extents. This is a similar qualitative feature observed in Figures 14 and 15 where a larger change in porosity and permeability was driven by uniformly propagating reactions over a distance from the origin. In comparison to the macroscopic porosity-permeability relationships, the precipitation reaction front is represented well by both common macroscopic relationships for both migration scenarios. However, the simulated change permeability for the dissolution regimes are over-estimated by macroscopic porosity-permeability relationships. The VermaPruess2 relationship is closer to simulated dissolution data than the Kozeny-Carman equation. These observations are similar to that of Chapter 2, Figure 5 where macroscopic relationships over-estimate simulated permeability values for uniform dissolution at 30% of relative pore and pore-throat size. The extent of change for permeability over porosity is larger than that resulting from a gradient front of reaction extents, where an observed increase of 2 normalized permeability values for dissolution and a decrease of 0.75 for precipitation scenarios for the uniform front migration scenario.

3.4 Conclusions

In this work, pore network modeling is used to simulate the effect of a migrating reaction front on porosity and permeability evolution. Fronts that results in uniform and gradient reaction extents are considered. Both scenarios simulate reactions occurring on all pore and pore-throat surfaces, altering radii by 30% relative to the unaltered pore and pore-throat sizes. Previous simulations of a sandstone sample (e.g. Chapter 2) consider the reactive region to include the entire network,

where in this work, the region migrates away from the origin to a given distance (e.g. x distance 10). Simulation results show the dependence of porosity-permeability evolution on the way reactions occur as a result of the migrating reaction front. For a given distance from the origin, reaction fronts that result in a uniform extent of reactions alter porosity and permeability more than if a gradient in reaction extent occurs, regardless of dissolution or precipitation reaction conditions. This is anticipated as the gradient reaction extent has a smaller reactive volume than the uniform reaction extent.

The changes in porosity and permeability for both reaction front migration scenarios are compared against common macroscopic porosity-permeability relationships, including Kozeny-Carman and Verma-Pruess. These common relationships are able to reflect precipitation reaction front migration scenarios, however, slightly overestimate the changes due to dissolution. Given that dissolution is most common in injection scenarios, this finding suggests a potential improvement to field-scale prediction of permeability, specifically in dissolution front migration scenarios.

Chapter 4

Conclusions and contributions to new knowledge

4.1. Effect of pore and pore-throat size distribution variations on porosity and permeability

In the first study presented, pore and pore-throat size distributions of a Viking sandstone sample, termed 3w4, from Beckingham et al. (2013) were altered to construct three synthetic distributions: left-skewed, normal and uniform pore and pore-throat size distributions. These three synthetic distributions and the 3w4 sample distributions, determined as right-skewed, reflect a large variation of sample characteristics resulting from discrepancies in characterization in laboratory or imaging analysis methods or sample properties. Pore network models were populated by sampling from each synthetic distribution and the porosity and permeability simulated and compared to each other and simulations from prior pore network modeling studies for sample 3w4 (Beckingham, 2017). Simulations considered the impact of uniform and non-uniform spatial distributions of mineral reactions on porosity and permeability. While earlier work in Beckingham (2017) observed that the spatial distribution of reactions within the pore network controls the evolution of porosity-permeability, the impact of variations in pore and pore-throat size distributions was unknown. No known previous study has analyzed simulated porosity-permeability for a wide range of pore and pore-throat size distributions given both uniform and non-uniform reaction scenarios. Results show that pore and pore-throat size distribution variations do not have a considerable impact on the qualitative nature of porosity-

permeability evolution, except for those that are driven by reactions initiated in either large or small pore and pore-throats.

4.2. A new modified Verma-Pruess relationship for size-dependent mineral reactions

Dissolution and precipitation reactions initiated in small or large pore and pore-throats result in a complex porosity-permeability evolution that is not reflected by common macroscopic porosity-permeability relationships. Macroscopic relationships such as Kozeny-Carman, Verma-Pruess and Fair-Hatch are implemented in field-scale studies of potential CO_2 injection sites, for example, and may risk the occurrence of major design errors if macroscopic relationships are unable to reflect changes in porous media at the pore-scale and in the greater network. Studies in Chapter 2 show that for reactions uniformly distributed throughout the pore matrix or in a fraction of network volume, macroscopic relationships are able to reflect the impact of dissolution and precipitation on porosity and permeability, for all pore and pore-throat size distributions considered. However, the phenomena observed for size-dependent mineral reactions at the pore-scale are not reflected in existing macroscopic porosity-permeability relationships. In this work, the Verma-Pruess relationship is modified and used to simulate changes in porosity and permeability for size-dependent mineral reaction scenarios. It is observed that this new modified Verma-Pruess equation is able to reflect the non-linear trend in porosity-permeability, regardless of pore and pore-throat distribution. For reactions initiated in large pores, constitutive porous media properties in dynamic reaction scenarios, such as a critical porosity where pore-throats become clogged or critical consolidated porosity where the sample become unconsolidated, is utilized in the modified relationship development. This allows the relationship to be less “empirical” by using physical and observable properties. For simulated

porosity-permeability given reactions initiated in small pores and pore-throats, the modified relationship is optimized and requires a fitting parameter. The value of this parameter depends on the fraction of small pores and pore-throats.

4.3. Impact of porosity-permeability evolution in mineral reaction propagations scenarios

Modification was made to the pore network model to analyze simulated porosity and permeability in scenarios where a reactive fluid migrates through the pore network, resulting in the propagation of dissolution and precipitation reactions. In future studies, variations in the spatial distribution of reactions and reaction extents will be analyzed as well as conditions where dissolution and precipitation occur in opposite ends of the network, demonstrating a scenario of mineral dissolution at inlet and reprecipitation at outlet. Preliminary simulation results show that a uniform front migration drives greater changes in both porosity and permeability than does a gradient front migration scenario. Common macroscopic relationships are able to reflect the change in reactive permeability for the precipitation front but slightly overestimate the permeability for the dissolution front. Suggestions for future work involves validation of model construction to ensure a proper representative elementary volume (REV) is obtained for each model network as front migration location increases. This current work includes the entire network domain (e.g. reactive region plus unreactive region) as reaction front migrates. Ideal model construction would limit the domain to only the reactive region comparing to simulations where reactions are throughout entire network domain, thus requiring a changing model matrix and REV. This work is intended to explore the change in porosity and permeability along the sample in a dynamic reaction condition and determine the total reactive volume required where little change is observed when compared to final porosity and permeability of a specific reactive

condition. This could be important for macroscopic relationship validation and better understanding the dynamic nature of porosity and permeability of a porous media in a migration front scenario.

References

Algive, L., Békri, S., Nader, F. H., Lerat, O., & Vizika, O. (2012). Impact of Diagenetic Alterations on the Petrophysical and Multiphase Flow Properties of Carbonate Rocks Using a Reactive Pore Network Modeling Approach. Oil & Gas Science and Technology – Revue d'IFP Energies nouvelles, 67, 147-160. doi: 10.2516/ogst/2011171

Al-Khulaifi, Y., Lin, Q., Blunt, M. J., & Bijeljic, B. (2018). Reservoir-condition pore-scale imaging of dolomite reaction with supercritical CO2acidified brine: Effect of pore-structure on reaction rate using velocity distribution analysis. International Journal of Greenhouse Gas Control, 68, 99-111. doi: 10.1016/j.ijggc.2017.11.011

Al-Yaseri, A., Zhang, Y., Ghasemiziarani, M., Sarmadivaleh, M., Lebedev, M., Roshan, H., & Iglauer, S. (2017). Permeability Evolution in Sandstone Due to CO2 Injection. Energy & Fuels, 31(11), 12390-12398. doi: 10.1021/acs.energyfuels.7b01701

Anovitz, L. M., & Cole, D. R. (2015). Characterization and Analysis of Porosity and Pore Structures. Reviews in Mineralogy and Geochemistry, 80, 61-164. doi: 10.2138/rmg.2015.80.04

Archer, D., Eby, M., Brovkin, V., Ridgwell, A., Cao, L., Mikolajewicz, U., ... & Tokos, K. (2009). Atmospheric lifetime of fossil fuel carbon dioxide. *Annual review of earth and planetary sciences*, *37*, 117-134.

Arns, J.-Y., Robins, V., Sheppard, A. P., Sok, R. M., Pinczewski, W. V., & Knackstedt, M. a. (2004). Effect of Network Topology on Relative Permeability. Transport in Porous Media, 55, 21-46. doi: 10.1023/B:TIPM.0000007252.68488.43

Bacci, G., Korre, A., & Durucan, S. (2011a). An experimental and numerical investigation into the impact of dissolution/precipitation mechanisms on CO2 injectivity in the wellbore and far field regions. *International Journal of Greenhouse Gas Control, 5*(3), 579-588. doi: 10.1016/j.ijggc.2010.05.007

Bacci, G., Korre, A., & Durucan, S. (2011b). Experimental investigation into salt precipitation during CO2 injection in saline aquifers. *Energy Procedia, 4*, 4450-4456. doi: 10.1016/j.egypro.2011.02.399

Bachu, S. (2000). Sequestration of CO2 in geological media: criteria and approach for site selection in response to climate change. *Energy conversion and management, 41*(9), 953-970.

Bachu, S. (2008). CO2storage in geological media: Role, means, status and barriers to deployment. *Progress in Energy and Combustion Science, 34*(2), 254-273. doi: 10.1016/j.pecs.2007.10.001

Bashtani, F., Taheri, S., & Kantzas, A. (2018). Scale up of pore-scale transport properties from micro to macro scale; network modelling approach. Journal of Petroleum Science and Engineering, 170, 541-562. doi: 10.1016/j.petrol.2018.07.001

Bear, J. (2013). Dynamics of fluids in porous media: Courier Corporation.

Beckingham, L. E. (2017). Evaluation of Macroscopic Porosity-Permeability Relationships in Heterogeneous Mineral Dissolution and Precipitation Scenarios. Water Resources Research, 217-230. doi: 10.1002/2017WR021306

Beckingham, L. E., Peters, C. A., Um, W., Jones, K. W., & Lindquist, W. B. (2013). 2D and 3D imaging resolution trade-offs in quantifying pore throats for prediction of permeability. Advances in Water Resources, 62, 1-12. doi: 10.1016/j.advwatres.2013.08.010

Bloomfield, J. P., Gooddy, D. C., Bright, M. I., & Williams, P. J. (2001). Pore-throat size distributions in Permo-Triassic sandstones from the United Kingdom and some implications for contaminant hydrogeology. Hydrogeology Journal, 9, 219-230. doi: 10.1007/s100400100135

Carman, P. C. (1997). Fluid flow through granular beds. Chemical Engineering Research and Design, 75, S32-S48. doi: 10.1016/S0263-8762(97)80003-2

Cil, M. B., Xie, M., Packman, A. I., & Buscarnera, G. (2017). Solute mixing regulates heterogeneity of mineral precipitation in porous media. Geophysical Research Letters, 44(13), 6658-6666.

Chadam, J., Hoff, D., Merino, E., Ortoleva, P., & Sen, A. (1986). Reactive infiltration instabilities. IMA Journal of Applied Mathematics (Institute of Mathematics and Its Applications), 36, 207-221. doi: 10.1093/imamat/36.3.207

Chen, X., & Yao, G. (2017). An improved model for permeability estimation in low permeable porous media based on fractal geometry and modified Hagen-Poiseuille flow. Fuel, 210, 748-757. doi: 10.1016/j.fuel.2017.08.101

Costa, A. (2006). Permeability-porosity relationship: A reexamination of the Kozeny-Carman equation based on a fractal pore-space geometry assumption. Geophysical Research Letters, 33, 1-5. doi: 10.1029/2005GL025134

Crandell, L. E., Peters, C. A., Um, W., Jones, K. W., & Lindquist, W. B. (2012). Changes in the pore network structure of Hanford sediment after reaction with caustic tank wastes. Journal of Contaminant Hydrology, 131, 89-99. doi: 10.1016/j.jconhyd.2012.02.002

Deng, H., Fitts, J. P., Crandall, D., McIntyre, D., & Peters, C. A. (2015). Alterations of fractures in carbonate rocks by CO2-acidified brines. Environmental science & technology, 49(16), 10226-10234.

Doyen, P. M. (1988). Permeability, conductivity, and pore geometry of sandstone. Journal of Geophysical Research, 93, 7729-7740. doi: 10.1029/JB093iB07p07729

Dvorkin, J., & Nur, A. (2002). Critical-porosity models. MEMOIRS-AMERICAN ASSOCIATION OF PETROLEUM GEOLOGISTS, 33-42.

Egermann, P., Bazin, B., & Vizika, O. (2005, January). An experimental investigation of reaction-transport phenomena during CO2 injection. In *SPE Middle East Oil and Gas Show and Conference*. Society of Petroleum Engineers.

Emmanuel, S., Ague, J. J., & Walderhaug, O. (2010). Interfacial energy effects and the evolution of pore size distributions during quartz precipitation in sandstone. Geochimica et Cosmochimica Acta, 74, 3539-3552. doi: 10.1016/j.gca.2010.03.019

Fatt, I. (1956). The Network Model of Porous Media. Petroleum Transactions, AIME, 207, 144-181.

Figueroa, J. D., Fout, T., Plasynski, S., McIlvried, H., & Srivastava, R. D. (2008). Advances in CO2 capture technology-The U.S. Department of Energy's Carbon Sequestration Program. *International Journal of Greenhouse Gas Control, 2*(1), 9-20. doi: 10.1016/s1750-5836(07)00094-1

Garcia-Rios, M., Luquot, L., Soler, J. M., & Cama, J. (2015). Influence of the flow rate on dissolution and precipitation features during percolation of CO2-rich sulfate solutions through fractured limestone samples. *Chemical Geology, 414,* 95-108. doi: 10.1016/j.chemgeo.2015.09.005

Gíslason, S. R., Sigurdardóttir, H., Aradóttir, E. S., & Oelkers, E. H. (2018). A brief history of CarbFix: Challenges and victories of the project's pilot phase. *Energy Procedia, 146,* 103-114. doi: 10.1016/j.egypro.2018.07.014

Golfier, F., Zarcone, C., Bazin, B., Lenormand, R., Lasseux, D., & Quintard, M. (2002). On the ability of a Darcy-scale model to capture wormhole formation during the dissolution of a porous medium. Journal of Fluid Mechanics, 457, 213-254. doi: 10.1017/S0022112002007735

Gouze, P., & Luquot, L. (2011). X-ray microtomography characterization of porosity, permeability and reactive surface changes during dissolution. Journal of Contaminant Hydrology, 120-121, 44-55. doi: 10.1016/j.jconhyd.2010.07.004

Hansen, J., Nazarenko, L., Ruedy, R., Sato, M., Willis, J., Del Genio, A., ... & Novakov, T. (2005). Earth's energy imbalance: Confirmation and implications. *science*, *308*(5727), 1431-1435.

Hao, Y., Smith, M., Sholokhova, Y., & Carroll, S. (2013). CO2-induced dissolution of low permeability carbonates. Part II: Numerical modeling of experiments. Advances in Water Resources, 62, 388-408. doi: 10.1016/j.advwatres.2013.09.009

Hodneland, E., Gasda, S., Kaufmann, R., Bekkvik, T. C., Hermanrud, C., & Midttømme, K. (2019). Effect of temperature and concentration of impurities in the fluid stream on CO2 migration in the Utsira formation. *International Journal of Greenhouse Gas Control*, *83*(December 2017), 20-28. doi: 10.1016/j.ijggc.2019.01.020

IPCC, 2000 – Robert T. Watson, Ian R. Noble, Bert Bolin, N. H. Ravindranath, David J. Verardo and David J. Dokken (Eds.) Cambridge University Press, UK. pp 375 Available from Cambridge University Press, The Edinburgh Building Shaftesbury Road, Cambridge CB2 2RU ENGLAND

IPCC, 2005 – Bert Metz, Ogunlade Davidson, Heleen de Coninck, Manuela Loos and Leo Meyer (Eds.) Cambridge University Press, UK. pp 431. Available from Cambridge University Press, The Edinburgh Building Shaftesbury Road, Cambridge CB2 2RU ENGLAND

IPCC, 2007: Climate Change 2007: Synthesis Report. Contribution of Working Groups I, II and III to the Fourth Assessment Report of the Intergovernmental Panel on Climate Change [Core Writing Team, Pachauri, R.K and Reisinger, A. (eds.)]. IPCC, Geneva, Switzerland, 104 pp.

Ishibashi, T., McGuire, T. P., Watanabe, N., Tsuchiya, N., & Elsworth, D. (2013). Permeability evolution in carbonate fractures: Competing roles of confining stress and fluid pH. Water Resources Research, 49, 2828-2842. doi: 10.1002/wrcr.20253

Jayne, R. S., Wu, H., & Pollyea, R. M. (2019). Geologic CO2 sequestration and permeability uncertainty in a highly heterogeneous reservoir. *International Journal of Greenhouse Gas Control*, *83*(October 2018), 128-139. doi: 10.1016/j.ijggc.2019.02.001

Jeddizahed, J., & Rostami, B. (2016). Experimental investigation of injectivity alteration due to salt precipitation during CO2 sequestration in saline aquifers. *Advances in Water Resources*, *96*, 23-33. doi: 10.1016/j.advwatres.2016.06.014

Keeling, C. D., Bacastow, R. B., Bainbridge, A. E., Ekdahl Jr, C. A., Guenther, P. R., Waterman, L. S., & Chin, J. F. (1976). Atmospheric carbon dioxide variations at Mauna Loa observatory, Hawaii. *Tellus*, *28*(6), 538-551.

Ketzer, J. M., Iglesias, R., Einloft, S., Dullius, J., Ligabue, R., & de Lima, V. (2009). Water-rock-CO2 interactions in saline aquifers aimed for carbon dioxide storage: Experimental and numerical modeling studies of the Rio Bonito Formation (Permian), southern Brazil. Applied Geochemistry, 24, 760-767. doi: 10.1016/j.apgeochem.2009.01.001

Khather, M., Saeedi, A., Rezaee, R., Noble, R. R. P., & Gray, D. (2017). Experimental investigation of changes in petrophysical properties during CO2injection into dolomite-rich rocks. International Journal of Greenhouse Gas Control, 59, 74-90. doi: 10.1016/j.ijggc.2017.02.007

Kim, D., Peters, C. A., & Lindquist, W. B. (2011). Upscaling geochemical reaction rates accompanying acidic CO 2-saturated brine flow in sandstone aquifers. Water Resources Research, 47, 1-16. doi: 10.1029/2010WR009472

Lai, J., Wang, G., Wang, Z., Chen, J., Pang, X., Wang, S., . . . Fan, X. (2017). A review on pore structure characterization in tight sandstones. Earth-Science Reviews, 177, 436-457. doi: 10.1016/j.earscirev.2017.12.003

Lamy-Chappuis, B., Yardley, B. W. D., He, S., Zu, Y., & Xie, J. (2018). A test of the effectiveness of pore scale fluid flow simulations and constitutive equations for modelling the effects of mineral dissolution on rock permeability. *Chemical Geology*, *483*(March), 501-510. doi: 10.1016/j.chemgeo.2018.03.020

Li, L., Peters, C. A., & Celia, M. A. (2006). Upscaling geochemical reaction rates using pore-scale network modeling. Advances in Water Resources, 29, 1351-1370. doi: 10.1016/j.advwatres.2005.10.011

Li, L., Peters, C. A., & Celia, M. A. (2007). Effects of mineral spatial distribution on reaction rates in porous media. Water Resources Research, 43, 1-17. doi: 10.1029/2005WR004848

Lichtner, P. C., & Kang, Q. (2007). Upscaling pore-scale reactive transport equations using a multiscale continuum formulation. Water Resources Research, 43. doi: 10.1029/2006WR005664

Lindquist, W. B., Lee, S.-M., Coker, D. a., Jones, K. W., & Spanne, P. (1996). Medial axis analysis of void structure in three-dimensional tomographic images of porous media. Journal of Geophysical Research, 101, 8297. doi: 10.1029/95JB03039

Lindquist, W. B., & Venkatarangan, A. (2000). synchrotron X-ray tomographic images. 105.

Lindquist, W. B., Venkatarangan, A., Dunsmuir, J., & Wong, T.-f. (2000). Pore and throat size distributions measured from synchrotron X-ray tomographic images of Fontainebleau

sandstones. Journal of Geophysical Research: Solid Earth, 105(B9), 21509-21527. doi: 10.1029/2000jb900208

Liu, H. H., Zhang, G., Yi, Z. L., & Wang, Y. (2013). A permeability-change relationship in the dryout zone for CO2injection into saline aquifers. International Journal of Greenhouse Gas Control, 15, 42-47. doi: 10.1016/j.ijggc.2013.01.034

Luhmann, A. J., Kong, X. Z., Tutolo, B. M., Garapati, N., Bagley, B. C., Saar, M. O., & Seyfried, W. E. (2014). Experimental dissolution of dolomite by CO2-charged brine at 100°C and 150bar: Evolution of porosity, permeability, and reactive surface area. Chemical Geology, 380, 145-160. doi: 10.1016/j.chemgeo.2014.05.001

Luquot, L., Andreani, M., Gouze, P., & Camps, P. (2012). CO2 percolation experiment through chlorite/zeolite-rich sandstone (Pretty Hill Formation – Otway Basin–Australia). Chemical Geology, 294-295, 75-88. doi: 10.1016/j.chemgeo.2011.11.018

Luquot, L., & Gouze, P. (2009). Experimental determination of porosity and permeability changes induced by injection of CO2 into carbonate rocks. Chemical Geology, 265, 148-159. doi: 10.1016/j.chemgeo.2009.03.028

Mangane, P. O., Gouze, P., & Luquot, L. (2013). Permeability impairment of a limestone reservoir triggered by heterogeneous dissolution and particles migration during CO2-rich injection. *Geophysical Research Letters*, *40*(17), 4614-4619. doi: 10.1002/grl.50595

Menke, H. P., Bijeljic, B., Andrew, M. G., & Blunt, M. J. (2015). Dynamic three-dimensional pore-scale imaging of reaction in a carbonate at reservoir conditions. *Environmental Science and Technology*, *49*(7), 4407-4414. doi: 10.1021/es505789f

Menke, H. P., Andrew, M. G., Blunt, M. J., & Bijeljic, B. (2016). Reservoir condition imaging of reactive transport in heterogeneous carbonates using fast synchrotron tomography – Effect of initial pore structure and flow conditions. Chemical Geology, 428, 15-26. doi: 10.1016/j.chemgeo.2016.02.030

Menke, H. P., Bijeljic, B., & Blunt, M. J. (2017). Dynamic reservoir-condition microtomography of reactive transport in complex carbonates: Effect of initial pore structure and initial brine pH. *Geochimica et Cosmochimica Acta, 204*, 267-285. doi: 10.1016/j.gca.2017.01.053

National Academy of Sciences. 2014. *Climate Change: Evidence and Causes*. Washington, DC: The National Academies Press. https://doi.org/10.17226/18730.

Nagy, K. L., & Lasaga, A. C. (1992). Dissolution and precipitation kinetics of gibbsite at 80°C and pH 3: The dependence on solution saturation state. Geochimica et Cosmochimica Acta, 56, 3093-3111. doi: 10.1016/0016-7037(92)90291-P

Niu, Q., & Zhang, C. (2017). Joint inversion of NMR and SIP data to estimate pore size distribution of geomaterials. Geophysical Journal International, 212(3), 1791-1805.

Nogues, J. P., Fitts, J. P., Celia, M. A., & Peters, C. A. (2013). Permeability evolution due to dissolution and precipitation of carbonates using reactive transport modeling in pore networks. Water Resources Research, 49, 6006-6021. doi: 10.1002/wrcr.20486

Noiriel, C. (2004). Investigation of porosity and permeability effects from microstructure changes during limestone dissolution. Geophysical Research Letters, 31(24). doi: 10.1029/2004gl021572

Noiriel, C. (2015). Resolving Time-dependent Evolution of Pore-Scale Structure, Permeability and Reactivity using X-ray Microtomography. Reviews in Mineralogy and Geochemistry, 80, 247-285. doi: 10.2138/rmg.2015.80.08

Noiriel, C., Gouze, P., & Bernard, D. (2004). Investigation of porosity and permeability effects from microstructure changes during limestone dissolution. Geophysical Research Letters, 31, 1-4. doi: 10.1029/2004GL021572

Noiriel, C., Steefel, C. I., Yang, L., & Bernard, D. (2016). Effects of pore-scale precipitation on permeability and flow. Advances in Water Resources, 95, 125-137. doi: 10.1016/j.advwatres.2015.11.013

Nunes, J. P. P., Blunt, M. J., & Bijeljic, B. (2016). Journal of Geophysical Research : Solid Earth Pore-scale simulation of carbonate dissolution in micro-CT images. *Journal of Geophysical Research: Solid Earth*. doi: 10.1002/2015JB012117.Received

Oelkers, E. H., Gislason, S. R., & Matter, J. (2008). Mineral carbonation of CO2. *Elements*, *4*(5), 333-337. doi: 10.2113/gselements.4.5.333

Øren, P. E., & Bakke, S. (2003). Reconstruction of Berea sandstone and pore-scale modelling of wettability effects. Journal of Petroleum Science and Engineering, 39(3-4), 177-199. Okabe, H., & Blunt, M. J. (2004). Prediction of permeability for porous media reconstructed using multiple-point statistics. Physical Review E, 70(6), 066135.

Okabe, H., & Blunt, M. J. (2004). Prediction of permeability for porous media reconstructed using multiple-point statistics. Physical Review E, 70(6), 066135.

Peters, C. A. (2009). Accessibilities of reactive minerals in consolidated sedimentary rock: An imaging study of three sandstones. Chemical Geology, 265, 198-208. doi: 10.1016/j.chemgeo.2008.11.014

Peuble, S., Godard, M., Gouze, P., Leprovost, R., Martinez, I., & Shilobreeva, S. (2019). Control of CO2 on flow and reaction paths in olivine-dominated basements: An experimental study. *Geochimica et Cosmochimica Acta, 252*, 16-38. doi: 10.1016/j.gca.2019.02.007

Qajar, J., & Arns, C. H. (2016). Characterization of reactive flow-induced evolution of carbonate rocks using digital core analysis- part 1: Assessment of pore-scale mineral dissolution and deposition. *Journal of Contaminant Hydrology, 192*, 60-86. doi: 10.1016/j.jconhyd.2016.06.005

Qi, N., Chen, G., Fang, M., Li, B., Liang, C., Ren, X., & Zhang, K. (2018). Damköhler number-based research on dividing dissolution patterns in carbonate acidizing. Journal of Petroleum Science and Engineering, 170, 922-931. doi: 10.1016/j.petrol.2018.06.070

Raoof, A., & Hassanizadeh, S. M. (2009). A New Method for Generating Pore-Network Models of Porous Media. Transport in Porous Media, 81(3), 391-407. doi: 10.1007/s11242-009-9412-3

Rötting, T. S., Luquot, L., Carrera, J., & Casalinuovo, D. J. (2015). Changes in porosity, permeability, water retention curve and reactive surface area during carbonate rock dissolution. Chemical Geology, 403, 86-98. doi: 10.1016/j.chemgeo.2015.03.008

Shah, S. M., Gray, F., Crawshaw, J. P., & Boek, E. S. (2016). Micro-computed tomography pore-scale study of flow in porous media: Effect of voxel resolution. Advances in Water Resources, 95, 276-287. doi: 10.1016/j.advwatres.2015.07.012

Singh, M., Chaudhuri, A., Chu, S., Stau, P. H., & Pawar, R. J. (2019). Analysis of evolving capillary transition , gravitational fingering , and dissolution trapping of CO 2 in deep saline aquifers during continuous injection of supercritical CO 2. *International Journal of Greenhouse Gas Control*, *82*(July 2018), 1-38. doi: 10.1016/j.ijggc.2019.01.014

Smith, M. M., Sholokhova, Y., Hao, Y., & Carroll, S. A. (2013). CO2-induced dissolution of low permeability carbonates. Part I: Characterization and experiments. Advances in Water Resources, 62, 370-387. doi: 10.1016/j.advwatres.2013.09.008

Snæbjörnsdóttir, S., Oelkers, E. H., Mesfin, K., Aradóttir, E. S., Dideriksen, K., Gunnarsson, I., . . . Gislason, S. R. (2017). The chemistry and saturation states of subsurface fluids during the in situ mineralisation of CO2 and H2S at the CarbFix site in SW-Iceland. *International Journal of Greenhouse Gas Control*, *58*, 87-102. doi: 10.1016/j.ijggc.2017.01.007

Soulaine, C., Roman, S., Kovscek, A., & Tchelepi, H. A. (2017). Mineral dissolution and wormholing from a pore-scale perspective. Journal of Fluid Mechanics, 827, 457-483.

Steefel, C. I., Beckingham, L. E., & Landrot, G. (2015). Micro-Continuum Approaches for Modeling Pore-Scale Geochemical Processes. Reviews in Mineralogy and Geochemistry, 80, 217-246. doi: 10.2138/rmg.2015.80.07

Tao, L., Xiao, P., Qader, A., & Webley, P. A. (2019). CO2 capture from high concentration CO2 natural gas by pressure swing adsorption at the CO2CRC Otway site, Australia. *International Journal of Greenhouse Gas Control*, *83*(December 2018), 1-10. doi: 10.1016/j.ijggc.2018.12.025

Tartakovsky, A. M., Meakin, P., Scheibe, T. D., & Eichler West, R. M. (2007). Simulations of reactive transport and precipitation with smoothed particle hydrodynamics. Journal of Computational Physics, 222, 654-672. doi: 10.1016/j.jcp.2006.08.013

Tenthorey, E., & Scholz, C. H. (2002). Mapping secondary mineral formation in porous media using heavy metal tracers. 107, 1-13. doi: 10.1029/2000JB000109

Tenthorey, E., Boreham, C. J., Hortle, A. L., Underschultz, J. R., & Golding, S. D. (2011). Importance of mineral sequestration during CO2 gas migration: A case study from the Greater Gorgon area. *Energy Procedia*, *4*, 5074-5078. doi: 10.1016/j.egypro.2011.02.481

Valdes-Parada, F. J., Ochoa-Tapia, J. A., & Alvarez-Ramirez, J. (2009). Validity of the permeability Carman-Kozeny equation: A volume averaging approach. Physica A: Statistical Mechanics and its Applications, 388, 789-798. doi: 10.1016/j.physa.2008.11.024

Varloteaux, C., Békri, S., & Adler, P. M. (2013). Pore network modelling to determine the transport properties in presence of a reactive fluid: From pore to reservoir scale. Advances in Water Resources, 53, 87-100. doi: 10.1016/j.advwatres.2012.10.004

Verma, a., & Pruess, K. (1988). Thermohydrological conditions and silica redistribution near high-level nuclear wastes emplaced in saturated geological formations. Journal of Geophysical Research, 93, 1159. doi: 10.1029/JB093iB02p01159

Voltolini, M., & Ajo-Franklin, J. (2019). The effect of CO2-induced dissolution on flow properties in Indiana Limestone: An in situ synchrotron X-ray micro-tomography study. *International Journal of Greenhouse Gas Control*, *82*(December 2018), 38-47. doi: 10.1016/j.ijggc.2018.12.013

Voltolini, M., Kwon, T. H., & Ajo-Franklin, J. (2017). Visualization and prediction of supercritical CO2 distribution in sandstones during drainage: An in situ synchrotron X-ray micro-computed tomography study. *International Journal of Greenhouse Gas Control, 66*(October), 230-245. doi: 10.1016/j.ijggc.2017.10.002

Williams, G. A., Chadwick, R. A., & Vosper, H. (2018). Some thoughts on Darcy-type flow simulation for modelling underground CO2storage, based on the Sleipner CO2storage operation. *International Journal of Greenhouse Gas Control, 68*(November 2017), 164-175. doi: 10.1016/j.ijggc.2017.11.010

Xiao, D., Lu, S., Lu, Z., Huang, W., & Gu, M. (2016). Combining nuclear magnetic resonance and rate-controlled porosimetry to probe the pore-throat structure of tight sandstones. Petroleum Exploration and Development, 43, 1049-1059. doi: 10.1016/S1876-3804(16)30122-7

Xiao, D., Lu, S., Yang, J., Zhang, L., & Li, B. (2017). Classifying Multiscale Pores and Investigating Their Relationship with Porosity and Permeability in Tight Sandstone Gas Reservoirs. Energy and Fuels, 31, 9188-9200. doi: 10.1021/acs.energyfuels.7b01487

Xiong, Q., Baychev, T. G., & Jivkov, A. P. (2016). Review of pore network modelling of porous media : Experimental characterisations , network constructions and applications to reactive transport. 192, 101-117.

Xu, T., Kharaka, Y. K., Doughty, C., Freifeld, B. M., & Daley, T. M. (2010). Reactive transport modeling to study changes in water chemistry induced by CO2 injection at the Frio-I Brine Pilot. *Chemical Geology*, *271*(3-4), 153-164.

Yi, Z., Lin, M., Jiang, W., Zhang, Z., Li, H., & Gao, J. (2017). Pore network extraction from pore space images of various porous media systems. Water Resources Research, 53(4), 3424-3445.

Zhang, P., Lu, S., Li, J., Zhang, J., Xue, H., & Chen, C. (2017). Comparisons of SEM, Low-Field NMR, and Mercury Intrusion Capillary Pressure in Characterization of the Pore Size Distribution of Lacustrine Shale: A Case Study on the Dongying Depression, Bohai Bay Basin, China. Energy & Fuels, 31(9), 9232-9239.

Zhang, M., Zhang, Y., & Lichtner, P. (2017b). Evaluating model complexity in simulating supercritical CO2dissolution, leakage, footprint, and reservoir pressure for three-dimensional hierarchical aquifer. *International Journal of Greenhouse Gas Control, 64*(June), 284-299. doi: 10.1016/j.ijggc.2017.07.022